Study of $e^+e^- \to p\bar{p}$ using initial state radiation with *BABAR*

B. Aubert,[1] R. Barate,[1] D. Boutigny,[1] F. Couderc,[1] Y. Karyotakis,[1] J. P. Lees,[1] V. Poireau,[1] V. Tisserand,[1] A. Zghiche,[1] E. Grauges,[2] A. Palano,[3] M. Pappagallo,[3] A. Pompili,[3] J. C. Chen,[4] N. D. Qi,[4] G. Rong,[4] P. Wang,[4] Y. S. Zhu,[4] G. Eigen,[5] I. Ofte,[5] B. Stugu,[5] G. S. Abrams,[6] M. Battaglia,[6] D. S. Best,[6] D. N. Brown,[6] J. Button-Shafer,[6] R. N. Cahn,[6] E. Charles,[6] C. T. Day,[6] M. S. Gill,[6] A. V. Gritsan,[6,*] Y. Groysman,[6] R. G. Jacobsen,[6] R. W. Kadel,[6] J. A. Kadyk,[6] L. T. Kerth,[6] Yu. G. Kolomensky,[6] G. Kukartsev,[6] G. Lynch,[6] L. M. Mir,[6] P. J. Oddone,[6] T. J. Orimoto,[6] M. Pripstein,[6] N. A. Roe,[6] M. T. Ronan,[6] W. A. Wenzel,[6] M. Barrett,[7] K. E. Ford,[7] T. J. Harrison,[7] A. J. Hart,[7] C. M. Hawkes,[7] S. E. Morgan,[7] A. T. Watson,[7] M. Fritsch,[8] K. Goetzen,[8] T. Held,[8] H. Koch,[8] B. Lewandowski,[8] M. Pelizaeus,[8] K. Peters,[8] T. Schroeder,[8] M. Steinke,[8] J. T. Boyd,[9] J. P. Burke,[9] W. N. Cottingham,[9] D. Walker,[9] T. Cuhadar-Donszelmann,[10] B. G. Fulsom,[10] C. Hearty,[10] N. S. Knecht,[10] T. S. Mattison,[10] J. A. McKenna,[10] A. Khan,[11] P. Kyberd,[11] M. Saleem,[11] L. Teodorescu,[11] A. E. Blinov,[12] V. E. Blinov,[12] A. D. Bukin,[12] V. P. Druzhinin,[12] V. B. Golubev,[12] E. A. Kravchenko,[12] A. P. Onuchin,[12] S. I. Serednyakov,[12] Yu. I. Skovpen,[12] E. P. Solodov,[12] A. N. Yushkov,[12] M. Bondioli,[13] M. Bruinsma,[13] M. Chao,[13] S. Curry,[13] I. Eschrich,[13] D. Kirkby,[13] A. J. Lankford,[13] P. Lund,[13] M. Mandelkern,[13] R. K. Mommsen,[13] W. Roethel,[13] D. P. Stoker,[13] S. Abachi,[14] C. Buchanan,[14] S. D. Foulkes,[15] J. W. Gary,[15] O. Long,[15] B. C. Shen,[15] K. Wang,[15] L. Zhang,[15] D. del Re,[16] H. K. Hadavand,[16] E. J. Hill,[16] D. B. MacFarlane,[16] H. P. Paar,[16] S. Rahatlou,[16] V. Sharma,[16] J. W. Berryhill,[17] C. Campagnari,[17] A. Cunha,[17] B. Dahmes,[17] T. M. Hong,[17] M. A. Mazur,[17] J. D. Richman,[17] T. W. Beck,[18] A. M. Eisner,[18] C. J. Flacco,[18] C. A. Heusch,[18] J. Kroseberg,[18] W. S. Lockman,[18] G. Nesom,[18] T. Schalk,[18] B. A. Schumm,[18] A. Seiden,[18] P. Spradlin,[18] D. C. Williams,[18] M. G. Wilson,[18] J. Albert,[19] E. Chen,[19] G. P. Dubois-Felsmann,[19] A. Dvoretskii,[19] D. G. Hitlin,[19] J. S. Minamora,[19] I. Narsky,[19] T. Piatenko,[19] F. C. Porter,[19] A. Ryd,[19] A. Samuel,[19] R. Andreassen,[20] G. Mancinelli,[20] B. T. Meadows,[20] M. D. Sokoloff,[20] F. Blanc,[21] P. C. Bloom,[21] S. Chen,[21] W. T. Ford,[21] J. F. Hirschauer,[21] A. Kreisel,[21] U. Nauenberg,[21] A. Olivas,[21] W. O. Ruddick,[21] J. G. Smith,[21] K. A. Ulmer,[21] S. R. Wagner,[21] J. Zhang,[21] A. Chen,[22] E. A. Eckhart,[22] A. Soffer,[22] W. H. Toki,[22] R. J. Wilson,[22] F. Winklmeier,[22] Q. Zeng,[22] D. D. Altenburg,[23] E. Feltresi,[23] A. Hauke,[23] B. Spaan,[23] T. Brandt,[24] M. Dickopp,[24] V. Klose,[24] H. M. Lacker,[24] R. Nogowski,[24] S. Otto,[24] A. Petzold,[24] J. Schubert,[24] K. R. Schubert,[24] R. Schwierz,[24] J. E. Sundermann,[24] D. Bernard,[25] G. R. Bonneaud,[25] P. Grenier,[25,†] E. Latour,[25] S. Schrenk,[25] Ch. Thiebaux,[25] G. Vasileiadis,[25] M. Verderi,[25] D. J. Bard,[26] P. J. Clark,[26] W. Gradl,[26] F. Muheim,[26] S. Playfer,[26] Y. Xie,[26] M. Andreotti,[27] D. Bettoni,[27] C. Bozzi,[27] R. Calabrese,[27] G. Cibinetto,[27] E. Luppi,[27] M. Negrini,[27] L. Piemontese,[27] F. Anulli,[28] R. Baldini-Ferroli,[28] A. Calcaterra,[28] R. de Sangro,[28] G. Finocchiaro,[28] P. Patteri,[28] I. M. Peruzzi,[28,‡] M. Piccolo,[28] A. Zallo,[28] A. Buzzo,[29] R. Capra,[29] R. Contri,[29] M. Lo Vetere,[29] M. M. Macri,[29] M. R. Monge,[29] S. Passaggio,[29] C. Patrignani,[29] E. Robutti,[29] A. Santroni,[29] S. Tosi,[29] G. Brandenburg,[30] K. S. Chaisanguanthum,[30] M. Morii,[30] J. Wu,[30] R. S. Dubitzky,[31] J. Marks,[31] S. Schenk,[31] U. Uwer,[31] W. Bhimji,[32] D. A. Bowerman,[32] P. D. Dauncey,[32] U. Egede,[32] R. L. Flack,[32] J. R. Gaillard,[32] J. A. Nash,[32] M. B. Nikolich,[32] W. Panduro Vazquez,[32] X. Chai,[33] M. J. Charles,[33] W. F. Mader,[33] U. Mallik,[33] V. Ziegler,[33] J. Cochran,[34] H. B. Crawley,[34] L. Dong,[34] V. Eyges,[34] W. T. Meyer,[34] S. Prell,[34] E. I. Rosenberg,[34] A. E. Rubin,[34] J. I. Yi,[34] G. Schott,[35] N. Arnaud,[36] M. Davier,[36] X. Giroux,[36] G. Grosdidier,[36] A. Höcker,[36] F. Le Diberder,[36] V. Lepeltier,[36] A. M. Lutz,[36] A. Oyanguren,[36] T. C. Petersen,[36] S. Pruvot,[36] S. Rodier,[36] P. Roudeau,[36] M. H. Schune,[36] A. Stocchi,[36] W. F. Wang,[36] G. Wormser,[36] C. H. Cheng,[37] D. J. Lange,[37] D. M. Wright,[37] A. J. Bevan,[38] C. A. Chavez,[38] I. J. Forster,[38] J. R. Fry,[38] E. Gabathuler,[38] R. Gamet,[38] K. A. George,[38] D. E. Hutchcroft,[38] R. J. Parry,[38] D. J. Payne,[38] K. C. Schofield,[38] C. Touramanis,[38] F. Di Lodovico,[39] W. Menges,[39] R. Sacco,[39] C. L. Brown,[40] G. Cowan,[40] H. U. Flaecher,[40] M. G. Green,[40] D. A. Hopkins,[40] P. S. Jackson,[40] T. R. McMahon,[40] S. Ricciardi,[40] F. Salvatore,[40] D. N. Brown,[41] C. L. Davis,[41] J. Allison,[42] N. R. Barlow,[42] R. J. Barlow,[42] Y. M. Chia,[42] C. L. Edgar,[42] M. P. Kelly,[42] G. D. Lafferty,[42] M. T. Naisbit,[42] J. C. Williams,[42] C. Chen,[43] W. D. Hulsbergen,[43] A. Jawahery,[43] D. Kovalskyi,[43] C. K. Lae,[43] D. A. Roberts,[43] G. Simi,[43] G. Blaylock,[44] C. Dallapiccola,[44] S. S. Hertzbach,[44] R. Kofler,[44] X. Li,[44] T. B. Moore,[44] S. Saremi,[44] H. Staengle,[44] S. Y. Willocq,[44] R. Cowan,[45] K. Koeneke,[45] G. Sciolla,[45] S. J. Sekula,[45] M. Spitznagel,[45] F. Taylor,[45] R. K. Yamamoto,[45] H. Kim,[46] P. M. Patel,[46] S. H. Robertson,[46] A. Lazzaro,[47] V. Lombardo,[47] F. F. Palombo,[47] J. M. Bauer,[48] L. Cremaldi,[48] V. Eschenburg,[48] R. Godang,[48] R. Kroeger,[48] J. Reidy,[48] D. A. Sanders,[48] D. J. Summers,[48] H. W. Zhao,[48] S. Brunet,[49] D. Côté,[49] P. Taras,[49] F. B. Viaud,[49] H. Nicholson,[50] N. Cavallo,[51,§] G. De Nardo,[51] F. Fabozzi,[51,§] C. Gatto,[51] L. Lista,[51] D. Monorchio,[51] P. Paolucci,[51] D. Piccolo,[51] C. Sciacca,[51] M. Baak,[52] H. Bulten,[52] G. Raven,[52] H. L. Snoek,[52] L. Wilden,[52] C. P. Jessop,[53] J. M. LoSecco,[53] T. Allmendinger,[54] G. Benelli,[54] K. K. Gan,[54] K. Honscheid,[54] D. Hufnagel,[54] P. D. Jackson,[54] H. Kagan,[54] R. Kass,[54] T. Pulliam,[54] A. M. Rahimi,[54] R. Ter-Antonyan,[54] Q. K. Wong,[54] N. L. Blount,[55] J. Brau,[55] R. Frey,[55] O. Igonkina,[55] M. Lu,[55] C. T. Potter,[55] R. Rahmat,[55] N. B. Sinev,[55] D. Strom,[55] J. Strube,[55]

E. Torrence,[55] F. Galeazzi,[56] M. Margoni,[56] M. Morandin,[56] M. Posocco,[56] M. Rotondo,[56] F. Simonetto,[56] R. Stroili,[56] C. Voci,[56] M. Benayoun,[57] J. Chauveau,[57] P. David,[57] L. Del Buono,[57] Ch. de la Vaissière,[57] O. Hamon,[57] B. L. Hartfiel,[57] M. J. J. John,[57] Ph. Leruste,[57] J. Malclès,[57] J. Ocariz,[57] L. Roos,[57] G. Therin,[57] P. K. Behera,[58] L. Gladney,[58] J. Panetta,[58] M. Biasini,[59] R. Covarelli,[59] S. Pacetti,[59] M. Pioppi,[59] C. Angelini,[60] G. Batignani,[60] S. Bettarini,[60] F. Bucci,[60] G. Calderini,[60] M. Carpinelli,[60] R. Cenci,[60] F. Forti,[60] M. A. Giorgi,[60] A. Lusiani,[60] G. Marchiori,[60] M. Morganti,[60] N. Neri,[60] E. Paoloni,[60] M. Rama,[60] G. Rizzo,[60] J. Walsh,[60] M. Haire,[61] D. Judd,[61] D. E. Wagoner,[61] J. Biesiada,[62] N. Danielson,[62] P. Elmer,[62] Y. P. Lau,[62] C. Lu,[62] J. Olsen,[62] A. J. S. Smith,[62] A. V. Telnov,[62] F. Bellini,[63] G. Cavoto,[63] A. D'Orazio,[63] E. Di Marco,[63] R. Faccini,[63] F. Ferrarotto,[63] F. Ferroni,[63] M. Gaspero,[63] L. Li Gioi,[63] M. A. Mazzoni,[63] S. Morganti,[63] G. Piredda,[63] F. Polci,[63] F. Safai Tehrani,[63] C. Voena,[63] H. Schröder,[64] R. Waldi,[64] T. Adye,[65] N. De Groot,[65] B. Franek,[65] G. P. Gopal,[65] E. O. Olaiya,[65] F. F. Wilson,[65] R. Aleksan,[66] S. Emery,[66] A. Gaidot,[66] S. F. Ganzhur,[66] G. Graziani,[66] G. Hamel de Monchenault,[66] W. Kozanecki,[66] M. Legendre,[66] B. Mayer,[66] G. Vasseur,[66] Ch. Yèche,[66] M. Zito,[66] M. V. Purohit,[67] A. W. Weidemann,[67] J. R. Wilson,[67] T. Abe,[68] M. T. Allen,[68] D. Aston,[68] R. Bartoldus,[68] N. Berger,[68] A. M. Boyarski,[68] O. L. Buchmueller,[68] R. Claus,[68] J. P. Coleman,[68] M. R. Convery,[68] M. Cristinziani,[68] J. C. Dingfelder,[68] D. Dong,[68] J. Dorfan,[68] D. Dujmic,[68] W. Dunwoodie,[68] S. Fan,[68] R. C. Field,[68] T. Glanzman,[68] S. J. Gowdy,[68] T. Hadig,[68] V. Halyo,[68] C. Hast,[68] T. Hryn'ova,[68] W. R. Innes,[68] M. H. Kelsey,[68] P. Kim,[68] M. L. Kocian,[68] D. W. G. S. Leith,[68] J. Libby,[68] S. Luitz,[68] V. Luth,[68] H. L. Lynch,[68] H. Marsiske,[68] R. Messner,[68] D. R. Muller,[68] C. P. O'Grady,[68] V. E. Ozcan,[68] A. Perazzo,[68] M. Perl,[68] B. N. Ratcliff,[68] A. Roodman,[68] A. A. Salnikov,[68] R. H. Schindler,[68] J. Schwiening,[68] A. Snyder,[68] J. Stelzer,[68] D. Su,[68] M. K. Sullivan,[68] K. Suzuki,[68] S. K. Swain,[68] J. M. Thompson,[68] J. Va'vra,[68] N. van Bakel,[68] M. Weaver,[68] A. J. R. Weinstein,[68] W. J. Wisniewski,[68] M. Wittgen,[68] D. H. Wright,[68] A. K. Yarritu,[68] K. Yi,[68] C. C. Young,[68] P. R. Burchat,[69] A. J. Edwards,[69] S. A. Majewski,[69] B. A. Petersen,[69] C. Roat,[69] S. Ahmed,[70] M. S. Alam,[70] R. Bula,[70] J. A. Ernst,[70] B. Pan,[70] M. A. Saeed,[70] F. R. Wappler,[70] S. B. Zain,[70] W. Bugg,[71] M. Krishnamurthy,[71] S. M. Spanier,[71] R. Eckmann,[72] J. L. Ritchie,[72] A. Satpathy,[72] R. F. Schwitters,[72] J. M. Izen,[73] I. Kitayama,[73] X. C. Lou,[73] S. Ye,[73] F. Bianchi,[74] M. Bona,[74] F. Gallo,[74] D. Gamba,[74] M. Bomben,[75] L. Bosisio,[75] C. Cartaro,[75] F. Cossutti,[75] G. Della Ricca,[75] S. Dittongo,[75] S. Grancagnolo,[75] L. Lanceri,[75] L. Vitale,[75] V. Azzolini,[76] F. Martinez-Vidal,[76] R. S. Panvini,[77,‖] Sw. Banerjee,[78] B. Bhuyan,[78] C. M. Brown,[78] D. Fortin,[78] K. Hamano,[78] R. Kowalewski,[78] I. M. Nugent,[78] J. M. Roney,[78] R. J. Sobie,[78] J. J. Back,[79] P. F. Harrison,[79] T. E. Latham,[79] G. B. Mohanty,[79] H. R. Band,[80] X. Chen,[80] B. Cheng,[80] S. Dasu,[80] M. Datta,[80] A. M. Eichenbaum,[80] K. T. Flood,[80] M. T. Graham,[80] J. J. Hollar,[80] J. R. Johnson,[80] P. E. Kutter,[80] H. Li,[80] R. Liu,[80] B. Mellado,[80] A. Mihalyi,[80] A. K. Mohapatra,[80] Y. Pan,[80] M. Pierini,[80] R. Prepost,[80] P. Tan,[80] S. L. Wu,[80] Z. Yu,[80] and H. Neal[81]

(*BABAR* Collaboration)

[1]*Laboratoire de Physique des Particules, F-74941 Annecy-le-Vieux, France*
[2]*IFAE, Universitat Autonoma de Barcelona, E-08193 Bellaterra, Barcelona, Spain*
[3]*Università di Bari, Dipartimento di Fisica and INFN, I-70126 Bari, Italy*
[4]*Institute of High Energy Physics, Beijing 100039, China*
[5]*University of Bergen, Institute of Physics, N-5007 Bergen, Norway*
[6]*Lawrence Berkeley National Laboratory and University of California, Berkeley, California 94720, USA*
[7]*University of Birmingham, Birmingham, B15 2TT, United Kingdom*
[8]*Ruhr Universität Bochum, Institut für Experimentalphysik 1, D-44780 Bochum, Germany*
[9]*University of Bristol, Bristol BS8 1TL, United Kingdom*
[10]*University of British Columbia, Vancouver, British Columbia, Canada V6T 1Z1*
[11]*Brunel University, Uxbridge, Middlesex UB8 3PH, United Kingdom*
[12]*Budker Institute of Nuclear Physics, Novosibirsk 630090, Russia*
[13]*University of California at Irvine, Irvine, California 92697, USA*
[14]*University of California at Los Angeles, Los Angeles, California 90024, USA*
[15]*University of California at Riverside, Riverside, California 92521, USA*
[16]*University of California at San Diego, La Jolla, California 92093, USA*
[17]*University of California at Santa Barbara, Santa Barbara, California 93106, USA*
[18]*University of California at Santa Cruz, Institute for Particle Physics, Santa Cruz, California 95064, USA*
[19]*California Institute of Technology, Pasadena, California 91125, USA*
[20]*University of Cincinnati, Cincinnati, Ohio 45221, USA*
[21]*University of Colorado, Boulder, Colorado 80309, USA*
[22]*Colorado State University, Fort Collins, Colorado 80523, USA*
[23]*Universität Dortmund, Institut für Physik, D-44221 Dortmund, Germany*

[24]*Technische Universität Dresden, Institut für Kern-und Teilchenphysik, D-01062 Dresden, Germany*
[25]*Ecole Polytechnique, LLR, F-91128 Palaiseau, France*
[26]*University of Edinburgh, Edinburgh EH9 3JZ, United Kingdom*
[27]*Università di Ferrara, Dipartimento di Fisica and INFN, I-44100 Ferrara, Italy*
[28]*Laboratori Nazionali di Frascati dell'INFN, I-00044 Frascati, Italy*
[29]*Università di Genova, Dipartimento di Fisica and INFN, I-16146 Genova, Italy*
[30]*Harvard University, Cambridge, Massachusetts 02138, USA*
[31]*Universität Heidelberg, Physikalisches Institut, Philosophenweg 12, D-69120 Heidelberg, Germany*
[32]*Imperial College London, London, SW7 2AZ, United Kingdom*
[33]*University of Iowa, Iowa City, Iowa 52242, USA*
[34]*Iowa State University, Ames, Iowa 50011-3160, USA*
[35]*Universität Karlsruhe, Institut für Experimentelle Kernphysik, D-76021 Karlsruhe, Germany*
[36]*Laboratoire de l'Accélérateur Linéaire, F-91898 Orsay, France*
[37]*Lawrence Livermore National Laboratory, Livermore, California 94550, USA*
[38]*University of Liverpool, Liverpool L69 72E, United Kingdom*
[39]*Queen Mary, University of London, E1 4NS, United Kingdom*
[40]*University of London, Royal Holloway and Bedford New College, Egham, Surrey TW20 0EX, United Kingdom*
[41]*University of Louisville, Louisville, Kentucky 40292, USA*
[42]*University of Manchester, Manchester M13 9PL, United Kingdom*
[43]*University of Maryland, College Park, Maryland 20742, USA*
[44]*University of Massachusetts, Amherst, Massachusetts 01003, USA*
[45]*Massachusetts Institute of Technology, Laboratory for Nuclear Science, Cambridge, Massachusetts 02139, USA*
[46]*McGill University, Montréal, Québec, Canada H3A 2T8*
[47]*Università di Milano, Dipartimento di Fisica and INFN, I-20133 Milano, Italy*
[48]*University of Mississippi, University, Mississippi 38677, USA*
[49]*Université de Montréal, Physique des Particules, Montréal, Québec, Canada H3C 3J7*
[50]*Mount Holyoke College, South Hadley, Massachusetts 01075, USA*
[51]*Università di Napoli Federico II, Dipartimento di Scienze Fisiche and INFN, I-80126, Napoli, Italy*
[52]*NIKHEF, National Institute for Nuclear Physics and High Energy Physics, NL-1009 DB Amsterdam, The Netherlands*
[53]*University of Notre Dame, Notre Dame, Indiana 46556, USA*
[54]*Ohio State University, Columbus, Ohio 43210, USA*
[55]*University of Oregon, Eugene, Oregon 97403, USA*
[56]*Università di Padova, Dipartimento di Fisica and INFN, I-35131 Padova, Italy*
[57]*Universités Paris VI et VII, Laboratoire de Physique Nucléaire et de Hautes Energies, F-75252 Paris, France*
[58]*University of Pennsylvania, Philadelphia, Pennsylvania 19104, USA*
[59]*Università di Perugia, Dipartimento di Fisica and INFN, I-06100 Perugia, Italy*
[60]*Università di Pisa, Dipartimento di Fisica, Scuola Normale Superiore and INFN, I-56127 Pisa, Italy*
[61]*Prairie View A&M University, Prairie View, Texas 77446, USA*
[62]*Princeton University, Princeton, New Jersey 08544, USA*
[63]*Università di Roma La Sapienza, Dipartimento di Fisica and INFN, I-00185 Roma, Italy*
[64]*Universität Rostock, D-18051 Rostock, Germany*
[65]*Rutherford Appleton Laboratory, Chilton, Didcot, Oxon, OX11 0QX, United Kingdom*
[66]*DSM/Dapnia, CEA/Saclay, F-91191 Gif-sur-Yvette, France*
[67]*University of South Carolina, Columbia, South Carolina 29208, USA*
[68]*Stanford Linear Accelerator Center, Stanford, California 94309, USA*
[69]*Stanford University, Stanford, California 94305-4060, USA*
[70]*State University of New York, Albany, New York 12222, USA*
[71]*University of Tennessee, Knoxville, Tennessee 37996, USA*
[72]*University of Texas at Austin, Austin, Texas 78712, USA*
[73]*University of Texas at Dallas, Richardson, Texas 75083, USA*
[74]*Università di Torino, Dipartimento di Fisica Sperimentale and INFN, I-10125 Torino, Italy*
[75]*Università di Trieste, Dipartimento di Fisica and INFN, I-34127 Trieste, Italy*
[76]*IFIC, Universitat de Valencia-CSIC, E-46071 Valencia, Spain*
[77]*Vanderbilt University, Nashville, Tennessee 37235, USA*
[78]*University of Victoria, Victoria, British Columbia, Canada V8W 3P6*

[*]Also with the Johns Hopkins University, Baltimore, Maryland 21218, USA.
[†]Also at Laboratoire de Physique Corpusculaire, Clermont-Ferrand, France.
[‡]Also with Università di Perugia, Dipartimento di Fisica, Perugia, Italy.
[§]Also with Università della Basilicata, Potenza, Italy.

[79]*Department of Physics, University of Warwick, Coventry CV4 7AL, United Kingdom*
[80]*University of Wisconsin, Madison, Wisconsin 53706, USA*
[81]*Yale University, New Haven, Connecticut 06511, USA*
(Received 9 December 2005; published 25 January 2006)

The $e^+e^- \to p\bar{p}$ cross section is determined over a range of $p\bar{p}$ masses, from threshold to 4.5 GeV/c^2, by studying the $e^+e^- \to p\bar{p}\gamma$ process. The data set corresponds to an integrated luminosity of 232 fb^{-1}, collected with the *BABAR* detector at the PEP-II storage ring, at an e^+e^- center-of-mass energy of 10.6 GeV. The mass dependence of the ratio of electric and magnetic form factors, $|G_E/G_M|$, is measured for $p\bar{p}$ masses below 3 GeV/c^2; its value is found to be significantly larger than 1 for masses up to 2.2 GeV/c^2. We also measure $J/\psi \to p\bar{p}$ and $\psi(2S) \to p\bar{p}$ branching fractions and set an upper limit on $Y(4260) \to p\bar{p}$ production and decay.

DOI: 10.1103/PhysRevD.73.012005 PACS numbers: 13.66.Bc, 13.25.Gv, 13.40.Gp, 14.20.Dh

I. INTRODUCTION

The $e^+e^- \to p\bar{p}$ cross section and the proton form factor can be measured over a range of center-of-mass energies by studying the initial state radiation (ISR) process $e^+e^- \to p\bar{p}\gamma$ (Fig. 1). The emission of a photon in the initial state gives rise to the possibility of measuring the cross section of the nonradiative process $e^+e^- \to p\bar{p}$ over a range of effective center-of-mass energies, from the threshold $m = 2m_p = 1.88$ GeV/c^2 to the full e^+e^- center-of-mass energy ($\sqrt{s}$). The Born cross section for this process, integrated over the nucleon momenta, is given by

$$\frac{d^2\sigma_{e^+e^-\to p\bar{p}\gamma}(m)}{dm\,d\cos\theta^*_\gamma} = \frac{2m}{s} W(s, x, \theta^*_\gamma)\sigma_{p\bar{p}}(m), \qquad (1)$$

where m is the $p\bar{p}$ invariant mass, $x \equiv 2E^*_\gamma/\sqrt{s} = 1 - m^2/s$, and E^*_γ and θ^*_γ are the ISR photon energy and polar angle, respectively, in the e^+e^- center-of-mass frame.[1] The function $W(s, x, \theta^*_\gamma)$ [1],

$$W(s, x, \theta^*_\gamma) = \frac{\alpha}{\pi x}\left(\frac{2 - 2x + x^2}{\sin^2\theta^*_\gamma} - \frac{x^2}{2}\right), \qquad (2)$$

is the probability of ISR photon emission for $\theta^*_\gamma \gg m_e/\sqrt{s}$, where α is the fine-structure constant and m_e is the electron mass. The cross section for the $e^+e^- \to p\bar{p}$ process is given by

$$\sigma_{p\bar{p}}(m) = \frac{4\pi\alpha^2\beta C}{3m^2}\left[|G_M(m)|^2 + \frac{2m_p^2}{m^2}|G_E(m)|^2\right], \qquad (3)$$

with $\beta = \sqrt{1 - 4m_p^2/m^2}$, $C = y/(1 - e^{-y})$, and $y = \pi\alpha m_p/(\beta m)$ is the Coulomb correction factor [2], which makes the cross section nonzero at threshold. The cross section depends on the magnetic form factor (G_M) and the electric form factor (G_E); at threshold, $|G_E| = |G_M|$. The modulus of the ratio of electric and magnetic form factors can be determined from the distribution of θ_p, the angle between the proton momentum in the $p\bar{p}$ rest frame and the momentum of the $p\bar{p}$ system in the e^+e^- center-of-mass frame. This distribution can be expressed as a sum of terms proportional to $|G_M|^2$ and $|G_E|^2$. The full differential cross section for $e^+e^- \to p\bar{p}\gamma$ can be found, for example, in Ref. [3]. The θ_p dependencies of the G_E and G_M terms are reminiscent of the $\sin^2\theta_p$ and $1 + \cos^2\theta_p$ angular distributions for electric and magnetic form factors in the $e^+e^- \to p\bar{p}$ process.

Measurements of the $e^+e^- \to p\bar{p}$ cross section have been performed in e^+e^- experiments [4–9] with (20–30)% precision. The cross section and proton form factor were deduced assuming $|G_E| = |G_M|$, and the measured proton angular distributions [5,6] did not contradict this assumption. More precise measurements of the proton form factor have been performed in $p\bar{p} \to e^+e^-$ experiments [10–12]. In the PS170 experiment [10] at LEAR, the proton form factor was measured from threshold ($p\bar{p}$ annihilation at rest) up to a mass of 2.05 GeV/c^2. The ratio $|G_E/G_M|$ was measured using the angular dependence of the cross section and was found to be compatible with unity. The LEAR data show a strong dependence of the form factor on the $p\bar{p}$ mass near threshold, and very little dependence in the range 1.95–2.05 GeV/c^2. Analyses from Fermilab experiments E760 [11] and E835 [12] show a strong decrease in the form factor at higher masses, in agreement with perturbative QCD, which predicts a $\alpha_s^2(m^2)/m^4$ dependence.

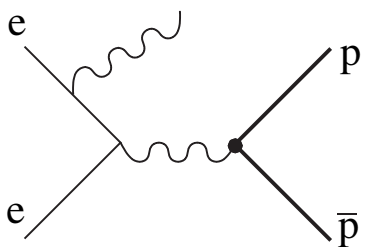

FIG. 1. The diagram for the $e^+e^- \to p\bar{p}\gamma$ process.

[1]Throughout this paper, the asterisk denotes quantities in the e^+e^- center-of-mass frame. All other variables except θ_p and θ_K are defined in the laboratory frame.

This work is an independent measurement by the *BABAR* Collaboration of the $e^+e^- \to p\bar{p}$ cross section $\sigma_{p\bar{p}}(m)$, for $p\bar{p}$ masses up to 4.5 GeV/c^2, based on the ISR process in e^+e^- annihilation at a fixed center-of-mass energy near 10.6 GeV. This study significantly improves the measurement of $\sigma_{p\bar{p}}(m)$ in the $p\bar{p}$ mass range up to 3 GeV/c^2. In contrast to previous e^+e^- and $p\bar{p}$ experiments, our measurement does not use the assumption that $|G_E| = |G_M|$. The ISR approach provides full θ_p coverage and hence high sensitivity to $|G_E/G_M|$. In this work, the mass dependence of the form-factor ratio $|G_E/G_M|$ is measured for $p\bar{p}$ masses below 3 GeV/c^2. We also study J/ψ and $\psi(2S)$ production in $e^+e^- \to p\bar{p}\gamma$, and measure the products $\Gamma(\psi \to e^+e^-)\mathcal{B}(\psi \to p\bar{p})$. A search for production of the $Y(4260)$ resonance, recently observed by *BABAR* in the ISR process $e^+e^- \to Y(4260)\gamma \to J/\psi\pi^+\pi^-\gamma$ [13], is performed.

II. THE *BABAR* DETECTOR AND DATA SAMPLES

We analyze a data sample corresponding to 232 fb^{-1} recorded with the *BABAR* detector [14] at the PEP-II asymmetric-energy storage ring. At PEP-II, 9-GeV electrons collide with 3.1-GeV positrons at a center-of-mass energy of 10.6 GeV [the $\Upsilon(4S)$ resonance].

Charged-particle tracking is provided by a five-layer silicon vertex tracker (SVT) and a 40-layer drift chamber (DCH), operating in a 1.5-T axial magnetic field. The transverse momentum resolution is 0.47% at 1 GeV/c. Energies of photons and electrons are measured with a CsI(Tl) electromagnetic calorimeter (EMC) with a resolution of 3% at 1 GeV. Charged-particle identification is provided by specific ionization (dE/dx) measurements in the SVT and DCH, and by an internally reflecting ring-imaging Cherenkov detector (DIRC). Muons are identified in the solenoid's instrumented flux return, which consists of iron plates interleaved with resistive plate chambers.

Signal and background ISR processes are simulated with Monte-Carlo (MC) event generators based on Ref. [15], with the differential cross section for $e^+e^- \to p\bar{p}\gamma$ taken from Ref. [3]. Because the polar-angle distribution of the ISR photon is peaked near 0° and 180°, the MC events are generated with a restriction on the photon polar angle: $20° < \theta^*_\gamma < 160°$, where θ^*_γ is measured in the e^+e^- center-of-mass frame. The extra soft-photon radiation from the initial state is generated with the structure function method [16]. To restrict the maximum energy of the extra photons, the invariant mass of the hadron system combined with the ISR photon is required to be at least 8 GeV/c^2. For background $e^+e^- \to \mu^+\mu^-\gamma$, $\pi^+\pi^-\gamma$, and $K^+K^-\gamma$ processes, final-state bremsstrahlung is generated using the PHOTOS package [17]. Background from $e^+e^- \to q\bar{q}$ is simulated with the JETSET [18] event generator. The response of the *BABAR* detector is simulated using the GEANT4 [19] program. The simulation takes into account the variation of the detector and accelerator conditions, and beam-induced background photons and charged particles overlapping events of interest.

III. EVENT SELECTION

The preselection of $e^+e^- \to p\bar{p}\gamma$ candidates requires that all the final-state particles are detected inside a fiducial volume. Since a significant fraction of the events contain beam-generated spurious tracks and photon candidates, we select events with at least two tracks with opposite charge and at least one photon candidate with $E^*_\gamma > 3$ GeV. The polar angle of the photon is required to be in the well-understood region of the calorimeter: $21.5° < \theta_\gamma < 137.5°$. The charged tracks must originate from the interaction point, have transverse momentum greater than 0.1 GeV/c, and be in the angular region between 25.8° and 137.5°, so that particle identification (PID) may be performed using the DIRC detector. To suppress background from radiative Bhabha events, events in which each of the two highest momentum tracks has a ratio of calorimetric energy deposition to momentum in the range 0.9 to 1.1 are rejected.

For events passing the preliminary selection, a kinematic fit is performed to the $e^+e^- \to C^+C^-\gamma$ hypothesis with requirements of total energy and momentum conservation. Here C can be e, μ, π, K, or p, and γ is the photon candidate with the highest energy in the e^+e^- center-of-mass frame. For events with more than two charged tracks, the fit uses the two oppositely charged tracks that pass closest to the interaction point. The Monte-Carlo simulation does not accurately reproduce the shape of the photon energy resolution function. This leads to a difference in the distributions of the χ^2 of the kinematic fit for data and for MC simulated events. To reduce this difference, only the measured direction of the ISR photon is used in the fit; its energy is treated as a free fit parameter. For each of the five charged-particle mass hypotheses, the corrected angles and energies of the particles and the χ^2 of the kinematic fit are calculated.

The selection of $e^+e^- \to p\bar{p}\gamma$ events relies upon both particle identification and event kinematics. The expected number of events from the background processes $e^+e^- \to \pi^+\pi^-\gamma$, $\mu^+\mu^-\gamma$, and $K^+K^-\gamma$ significantly exceeds the number of signal events (by 2 to 3 orders of magnitude). To suppress these backgrounds, both charged particles must be identified as protons according to the specific ionization (dE/dx) measured in the SVT and DCH, and the Cherenkov angle measured in the DIRC. These particle identification requirements lead to a loss of approximately 30% of the signal events, while suppressing backgrounds by factors of 15×10^3, 500×10^3, and 2×10^3 for pion, muon, and kaon events, respectively.

Background is further suppressed through requirements on the χ^2 of the kinematic fit: $\chi^2_p < 30$ and $\chi^2_K > 30$, where χ^2_p and χ^2_K are the χ^2 of the kinematic fit for the proton and kaon mass hypotheses, respectively. The distri-

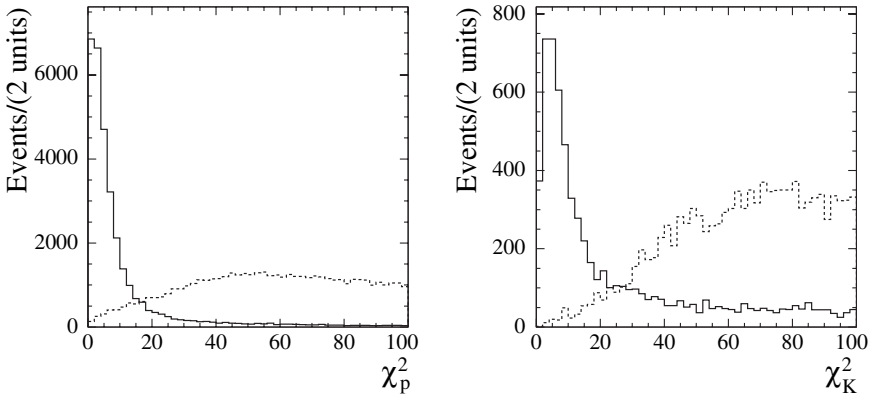

FIG. 2. The χ^2_p distribution (left panel) for MC simulated $e^+e^- \to p\bar{p}\gamma$ (solid line) and $e^+e^- \to K^+K^-\gamma$ (dashed line) events, and the χ^2_K distribution (right panel) for MC simulated $e^+e^- \to K^+K^-\gamma$ (solid line) and $e^+e^- \to p\bar{p}\gamma$ (dashed line) events with $\chi^2_p < 30$.

bution of χ^2_p for Monte-Carlo simulated $p\bar{p}\gamma$ events is shown in Fig. 2 (left panel). The long tail in the distribution at high χ^2 is due to events with extra photons emitted in the initial state. The dashed histogram is the χ^2_p distribution for $K^+K^-\gamma$ Monte-Carlo simulated events. Figure 2 (right panel) shows the distributions of χ^2_K for $K^+K^-\gamma$ and $p\bar{p}\gamma$ Monte-Carlo simulated events with $\chi^2_p < 30$. The χ^2 requirements lead to a loss of 25% of signal events but provides additional background suppression by a factor of 50 for $e^+e^- \to \pi^+\pi^-\gamma$ and $\mu^+\mu^-\gamma$ events, and a factor of 30 for $e^+e^- \to K^+K^-\gamma$ events.

The $p\bar{p}$ invariant mass distribution is shown in Fig. 3 for the ≈ 4000 events that satisfy all the selection criteria. Most of the events have invariant mass below 3 GeV/c^2. Clear signals from $J/\psi \to p\bar{p}$ and $\psi(2S) \to p\bar{p}$ decays are evident.

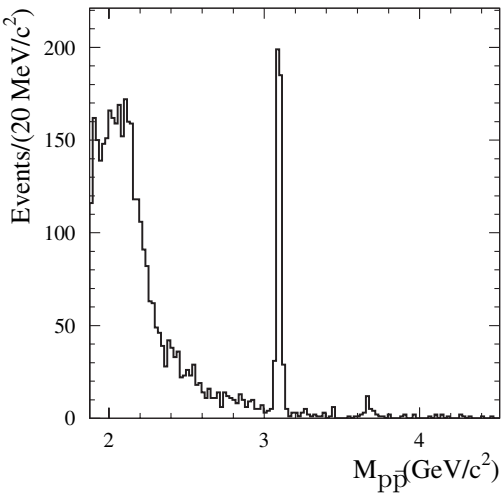

FIG. 3. The $p\bar{p}$ invariant mass spectrum for $p\bar{p}\gamma$ candidates that satisfy all selection criteria.

IV. BACKGROUND AND ITS SUBTRACTION

The possible sources of background in the sample of $e^+e^- \to p\bar{p}\gamma$ candidates that pass the selection criteria described in the previous section include $e^+e^- \to \pi^+\pi^-\gamma$, $e^+e^- \to K^+K^-\gamma$, $e^+e^- \to \mu^+\mu^-\gamma$, and $e^+e^- \to e^+e^-\gamma$ events in which the charged particles are misidentified as protons. Backgrounds from processes with protons plus neutral particle(s) in the final state are also anticipated: $e^+e^- \to p\bar{p}\pi^0$, $p\bar{p}\eta$, $p\bar{p}\pi^0\gamma$, etc.

Of particular interest is the possible background from the process $e^+e^- \to p\bar{p}\gamma$ with the photon emitted from the final state. Because of different charge parity of the amplitudes corresponding to initial state radiation and final-state radiation (FSR), their interference does not contribute to the total $e^+e^- \to p\bar{p}\gamma$ cross section. The contribution of the FSR amplitude is estimated to be [20] $d\sigma/dm \approx |F_{ax}|^2 8m\alpha^3\beta/(27s^2)$, where F_{ax} is the axial proton form factor. Assuming $|F_{ax}| \approx |G_M|$, the ratio of FSR to ISR cross sections is determined to be about 10^{-3} for $p\bar{p}$ masses below 4.5 GeV/c^2, implying that the FSR background is sufficiently small to neglect.

A. $e^+e^- \to \pi^+\pi^-\gamma$, $e^+e^- \to K^+K^-\gamma$, $e^+e^- \to \mu^+\mu^-\gamma$, and $e^+e^- \to e^+e^-\gamma$ backgrounds

To estimate the background contribution from $e^+e^- \to \pi^+\pi^-\gamma$, data and Monte-Carlo simulated events are selected with the following requirements on PID and on the χ^2 of the kinematic fits:

(1) one proton candidate, $\chi^2_\pi < 20$;
(2) one proton candidate, $\chi^2_p < 30$, $\chi^2_K > 30$;
(3) two proton candidates, $\chi^2_\pi < 20$;
(4) two proton candidates, $\chi^2_p < 30$, $\chi^2_K > 30$.

Here χ^2_π is the χ^2 of the kinematic fit for the pion-mass hypothesis.

The fourth set of conditions corresponds to the standard selection criteria for $p\bar{p}\gamma$ candidates. The invariant mass $M_{\pi\pi}$ of the two charged particles under the pion-mass

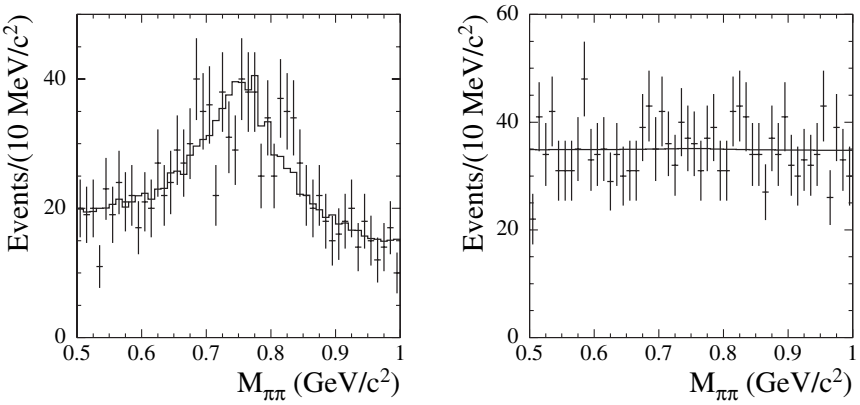

FIG. 4. The $M_{\pi\pi}$ spectrum for data events with $\chi^2_p < 30$ and $\chi^2_K > 30$, and one proton candidate (left plot; selection 2 in the text) or two proton candidates (right plot; selection 4 in the text). The histograms are the results of the fit described in the text.

hypothesis is calculated; the $M_{\pi\pi}$ distributions for data selected with criteria 2 and 4 are shown in Fig. 4. The ρ resonance in the $e^+e^- \to \pi^+\pi^-\gamma$ reaction is clearly seen in the distribution corresponding to selection 2 (left plot in Fig. 4). The number of $\pi\pi\gamma$ events with $0.5 < M_{\pi\pi} < 1$ GeV/c^2 passing each set of selection criteria is determined by fitting the $M_{\pi\pi}$ distribution with a $\pi\pi\gamma$ spectrum predicted by a Monte-Carlo simulation plus a first order polynomial to account for background from non-$\pi\pi\gamma$ processes. The Monte-Carlo $\pi\pi\gamma$ spectrum uses a model of the pion form factor based on existing experimental data. The results of the fits for $\pi\pi\gamma$ candidates passing selection criteria 1, 2, 3, and 4 are listed in Table I together with the corresponding numbers from the Monte-Carlo simulation.

Particle identification for the simulated $\pi\pi\gamma$ events is accomplished using two sets of information: fully simulated observables that are used for particle identification in the same manner as in the analysis of data, and event weights for the simulated events based on pion misidentification rates derived from a control sample of known pions in data. The identification based on event weights does not take into account possible correlations between pion misidentification probabilities for two particles that overlap in the detector, or that are in close proximity and therefore may underestimate the yield of wrongly identified $\pi\pi\gamma$ events. No events passing selection 4 are found in the fully simulated PID sample, and so a 90% confidence level (CL) upper limit is estimated for the standard selection (selection 4) in Table I. Because neither the fully simulated nor weighted PID samples predict the number of $\pi\pi\gamma$ events seen in the data passing selection 4, an estimate is made based on the number of data events passing selection 3: $N_4 = N_3/R_{\pi\pi}$, where $R_{\pi\pi}$ is the ratio of the number of candidates that satisfy $\chi^2_\pi < 20$ to the number that satisfy $\chi^2_p < 30$ and $\chi^2_K > 30$ (the numbers given in the first and second rows in Table I). The statistical uncertainty on the scale factor $R_{\pi\pi}$ from the simulation is about 20%. $R_{\pi\pi}$ estimated for events with one and two misidentified pions are consistent with each other. Accordingly, the scale factor ratio $R_{\pi\pi} = 35 \pm 9$ obtained from data is used, with an additional 30% systematic uncertainty assigned. Finally, N_4 is estimated as $N_4 = (190 \pm 30)/(35 \pm 14) = 5.4 \pm 2.3$. The fit with $N_4 = 5.4$, shown in Fig. 4, describes the mass distribution for selection 4 very well. The total number of $\pi\pi\gamma$ events remaining for the standard selection criteria is calculated as $N_{\pi\pi} = 1.1 \times N_4 = 5.9 \pm 2.5$, where 1.1 is the ratio of the total number of $\pi\pi\gamma$ events to those in the $0.5 < M_{\pi\pi} < 1$ GeV/c^2 mass region and is taken from simulation. The expected $M_{p\bar{p}}$ spectrum for $\pi\pi\gamma$ events passing the $p\bar{p}\gamma$ selection criteria is shown as the dotted histogram in Fig. 5.

TABLE I. The numbers of $\pi\pi\gamma$ events with $0.5 < M_{\pi\pi} < 1$ GeV/c^2 passing different selection criteria for data and MC simulation. WMC denotes Monte-Carlo simulation with data-derived particle identification weights. The data numbers are obtained from the fit of the $M_{\pi\pi}$ distributions as described in the text. $R_{\pi\pi}$ is the ratio of the numbers of events in the previous two rows.

	One proton candidate			Two proton candidates		
	Data	MC	WMC	Data	MC	WMC
$N(\chi^2_\pi < 20)$	16200 ± 200	21020 ± 230	12300 ± 300	190 ± 30	246 ± 25	35.5 ± 0.8
$N(\chi^2_p < 30, \chi^2_K > 30)$	460 ± 120	590 ± 40	300 ± 5	...	<5.7	0.90 ± 0.03
$R_{\pi\pi}$	35 ± 9	36 ± 2	43 ± 1	...	>43	39 ± 2

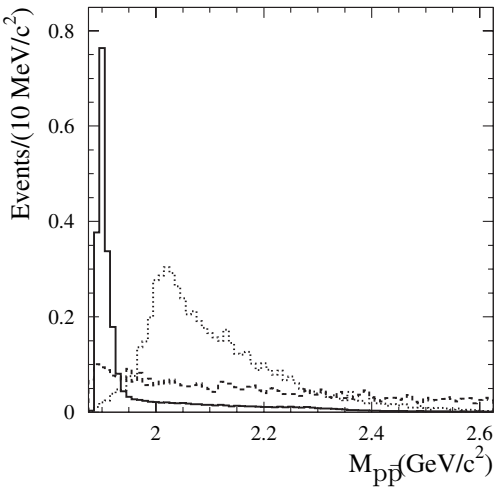

FIG. 5. The calculated $M_{p\bar{p}}$ spectra for $e^+e^- \to \pi^+\pi^-\gamma$ (dotted histogram), $e^+e^- \to K^+K^-\gamma$ (solid histogram), and $e^+e^- \to \mu^+\mu^-\gamma$ (dashed histogram) background processes. The spectra are normalized to the number of events expected to pass the $p\bar{p}\gamma$ selection criteria for each process: 5.9 ± 2.5 for pions and 2.5 ± 1.0 for kaons. For the muon channel, the upper limit of 11 events is used for the normalization.

The procedure used to estimate the background from the $e^+e^- \to K^+K^-\gamma$ process is similar to that used to estimate the $e^+e^- \to \pi^+\pi^-\gamma$ background. The number of events in the ϕ meson peak in the distribution of invariant mass of the charged particles calculated under the kaon hypothesis is used to determine the number of kaon events. The total number of $KK\gamma$ events remaining after the standard selection criteria is estimated to be $N_{KK} = 2.5 \pm 1.0$. The expected $M_{p\bar{p}}$ distribution for these events is shown as the solid histogram in Fig. 5.

To estimate the electron background, the kinematic properties of the $e^+e^- \to e^+e^-\gamma$ process are used. About 60% of $e^+e^-\gamma$ events have e^+e^- invariant mass between 3 and 7 GeV/c^2 and $\cos\psi^* < -0.97$, where ψ^* is the angle between the two tracks in the e^+e^- center-of-mass frame. In the event sample with two proton candidates, only one event has the above characteristics. With this event assumed to be background from $e^+e^- \to e^+e^-\gamma$, the total $e^+e^-\gamma$ background is estimated to be 1.8 ± 1.8 (0.8 events with $M_{p\bar{p}} < 4.5$ GeV/c^2).

The method used to estimate $\mu^+\mu^-\gamma$ background relies on the difference between the two-proton and the two-muon mass spectra. From the simulation 44% of $\mu^+\mu^-\gamma$ events are expected to have a two-proton invariant mass greater than 4.5 GeV. In data, only four such events are found, with an expected background of 5 ± 3 events from the $e^+e^- \to p\bar{p}\pi^0$ process (see Sec. IV B). From these numbers, the total muon background is estimated to not exceed 11 events. A similar limit is obtained directly from $\mu^+\mu^-\gamma$ Monte-Carlo simulation. From about 2×10^6 simulated $\mu^+\mu^-\gamma$ events (20% of the number of events expected in data), no events pass the $p\bar{p}\gamma$ selection criteria, leading to a 90% CL upper limit of 12 events. The expected $M_{p\bar{p}}$ spectrum for $e^+e^- \to \mu^+\mu^-\gamma$ events normalized to a total of 11 events is shown as the dashed histogram in Fig. 5. This upper limit on the number of muon events is used as a measure of the systematic uncertainty due to $\mu^+\mu^-\gamma$ background. This uncertainty is calculated as a function of the $p\bar{p}$ mass and is added to the systematic error on the number of $p\bar{p}\gamma$ events.

B. $e^+e^- \to p\bar{p}\pi^0$ background

A dominant source of background to the $e^+e^- \to p\bar{p}\gamma$ process arises from $e^+e^- \to p\bar{p}\pi^0$. A significant fraction of $p\bar{p}\pi^0$ events with an undetected low-energy photon or with merged photons from the π^0 decay are reconstructed under the $p\bar{p}\gamma$ hypothesis with a low value of χ^2 and thus are not easily separable from the process under study. Experimental data is used to devise a procedure to subtract this background.

For the $p\bar{p}\pi^0$ background study, events with two charged particles identified as protons and at least two photons with energy greater than 0.1 GeV, one of which must have center-of-mass energy above 3 GeV, are selected. The two-photon invariant mass is required to be in the range 0.07 to 0.2 GeV/c^2. A kinematic fit under the $e^+e^- \to p\bar{p}\gamma\gamma$ hypothesis is then performed. For events with more than two photons, all two-photon combinations are analyzed and only the combination with the smallest χ^2 in the kinematic fit is considered. Requirements on the χ^2 of the kinematic fit ($\chi^2 < 25$) and the two-photon invariant mass ($0.1025 < M_{\gamma\gamma} < 0.1675$ GeV/c^2) are then imposed on the $e^+e^- \to p\bar{p}\pi^0$ candidates. The sidebands $0.0700 < M_{\gamma\gamma} < 0.1025$ GeV/c^2 and $0.1675 < M_{\gamma\gamma} < 0.2000$ GeV/c^2 are used to estimate background. The $M_{p\bar{p}}$ spectra and $\cos\theta_p$ distributions for data events from the signal and sideband regions are shown in Fig. 6. The total number of selected events is 74 in the signal region and 10 in the sidebands. The number of $e^+e^- \to p\bar{p}\pi^0$ events in the sidebands expected from MC simulation is 2.7.

The $p\bar{p}\gamma\gamma$ selection criteria described above are applied to simulated $e^+e^- \to q\bar{q}$ events generated with the JETSET package. The predicted number of $e^+e^- \to p\bar{p}\pi^0$ events is 73 ± 7. These events have an enhancement in the $M_{p\bar{p}}$ distribution near $p\bar{p}$ threshold, similar to that in data (Fig. 6), but the angular distribution is peaked at $\cos\theta_p = \pm 1$ and is not consistent with the nearly flat distribution found in data. To study these events, simulated $e^+e^- \to p\bar{p}\pi^0$ events are generated according to three-body phase space with an additional weight proportional to $(M_{p\bar{p}} - 1.86)^{3/2}$ (to imitate the $M_{p\bar{p}}$ distribution observed in data). The resulting $\cos\theta_p$ distribution is flat. With these simulated events, $K_{\rm MC}(M_{p\bar{p}})$ is calculated as the ratio of the $M_{p\bar{p}}$ distributions for events selected with the standard

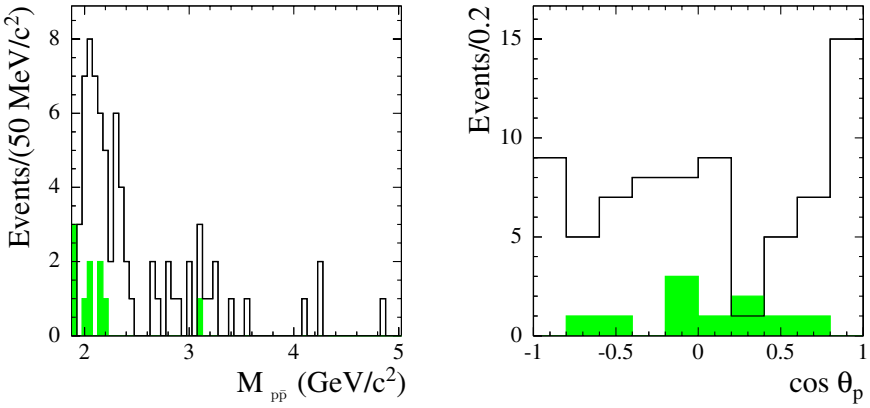

FIG. 6 (color online). The $M_{p\bar{p}}$ spectrum (left panel) and the $\cos\theta_p$ distribution (right panel) for selected $e^+e^- \to p\bar{p}\pi^0$ candidates in data. The shaded histogram shows the background contribution estimated from $M_{\gamma\gamma}$ sidebands.

$p\bar{p}\gamma$ criteria to those with the $p\bar{p}\pi^0$ criteria as a function of $M_{p\bar{p}}$. The value of the ratio $K_{\rm MC}(M_{p\bar{p}})$ varies between 3.7 near $M_{p\bar{p}}$ threshold to 2.0 at 5 GeV/c^2. The expected $M_{p\bar{p}}$ spectrum for $e^+e^- \to p\bar{p}\pi^0$ background passing the $p\bar{p}\gamma$ selection criteria is shown in Fig. 7 and is evaluated as $K_{\rm MC}(M_{p\bar{p}}) \times (dN/dM_{p\bar{p}})_{\rm data}$, where $(dN/dM_{p\bar{p}})_{\rm data}$ is the mass distribution for $e^+e^- \to p\bar{p}\pi^0$ events obtained above (Fig. 6). In Table II, the number of selected $e^+e^- \to p\bar{p}\gamma$ candidates and the expected number of $e^+e^- \to p\bar{p}\pi^0$ background events for different $p\bar{p}$ mass ranges are given. [The $p\bar{p}$ mass ranges near the J/ψ and $\psi(2S)$ resonances are excluded.] The background contribution grows from 5% near $p\bar{p}$ threshold to 40% at $M_{p\bar{p}} \approx 4$ GeV/c^2. All observed $p\bar{p}\gamma$ candidates with $M_{p\bar{p}} > 4.5$ GeV/c^2 are consistent with $p\bar{p}\pi^0$ background.

The JETSET simulation is used to find other possible sources of background from $e^+e^- \to q\bar{q}$. The number of

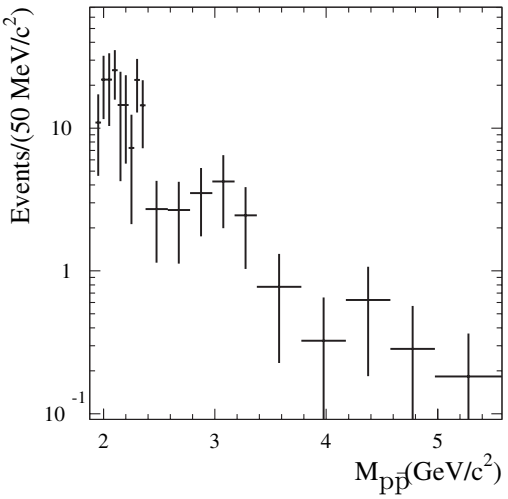

FIG. 7. The expected $M_{p\bar{p}}$ spectrum for $e^+e^- \to p\bar{p}\pi^0$ events selected with the standard $p\bar{p}\gamma$ criteria. The spectrum is obtained by scaling the data distribution shown in Fig. 6 by the factor $K_{\rm MC}(M_{p\bar{p}})$ described in the text.

$q\bar{q}$ events with final states other than $p\bar{p}\pi^0$ passing all cuts is 26 ± 4, with two final states, $p\bar{p}2\pi^0$ and $p\bar{p}\eta$, accounting for 17 and 5 events, respectively. The background contribution from these sources is estimated from data using the χ^2 sideband as described below.

C. $e^+e^- \to p\bar{p}\pi^0\gamma$ background

The dominant ISR background process with protons in the final state is $e^+e^- \to p\bar{p}\pi^0\gamma$. To estimate this background, events are selected with two charged particles identified as protons and at least three photons with energy greater than 0.1 GeV, with one of these photons having center-of-mass energy above 3 GeV. The invariant mass of the two least energetic photons is required to be in the range 0.07–0.20 GeV/c^2. For events that pass these criteria, a kinematic fit under the $e^+e^- \to p\bar{p}\pi^0\gamma$ hypothesis is performed. The distribution of $p\bar{p}\pi^0$ invariant mass for events with $\chi^2 < 20$ is shown in Fig. 8 (left panel). The shaded histogram shows the background contribution estimated from the χ^2 sideband: $30 < \chi^2 < 50$. Most $e^+e^- \to p\bar{p}\pi^0\gamma$ events have a $p\bar{p}\pi^0$ mass near a peak at 2.6 GeV. The contribution of the $J/\psi \to p\bar{p}\pi^0$ decay is also seen. The $p\pi^0$ ($\bar{p}\pi^0$) mass spectrum for events with $p\bar{p}\pi^0$ mass away from the J/ψ resonance is shown in Fig. 8 (right panel). The mass and width of the peak dominating in this distribution agree with the parameters of the $N(1440)$ state, suggesting that the main mechanism in the $e^+e^- \to p\bar{p}\pi^0$ reaction is a transition through $N(1440)\bar{p}$ or $\bar{N}(1440)p$ intermediate states.

TABLE II. The number of selected $p\bar{p}\gamma$ candidates, $N_{p\bar{p}\gamma}$, and the number of background events from the $e^+e^- \to p\bar{p}\pi^0$ process, $N_{p\bar{p}\pi^0}$, for different ranges of $M_{p\bar{p}}$. The $p\bar{p}$ mass ranges near the J/ψ and $\psi(2S)$ resonances are excluded.

$M_{p\bar{p}}$ (GeV/c^2)	<2.50	2.50–3.05	3.15–3.60	3.75–4.50	>4.5
$N_{p\bar{p}\gamma}$	3166	322	37	20	4
$N_{p\bar{p}\pi^0}$	171 ± 29	33 ± 11	17 ± 7	8 ± 4	5 ± 3

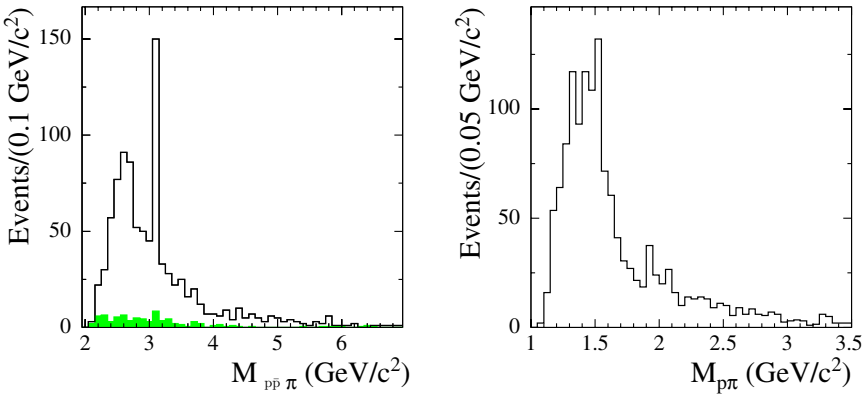

FIG. 8 (color online). Left panel: the $p\bar{p}\pi^0$ mass spectrum for selected $e^+e^- \to p\bar{p}\pi^0\gamma$ candidates with $\chi^2 < 20$. The shaded histogram shows the background contribution estimated from the sideband with $30 < \chi^2 < 50$. Right panel: the $p\pi^0$ ($\bar{p}\pi^0$) mass spectrum for $e^+e^- \to p\bar{p}\pi^0\gamma$ data events with $p\bar{p}\pi^0$ mass outside the J/ψ peak.

The number of $e^+e^- \to p\bar{p}\pi^0\gamma$ events passing the $p\bar{p}\gamma$ selection is estimated using Monte-Carlo simulation; $e^+e^- \to p\bar{p}\pi^0\gamma$ events are generated in the $N(1440)\bar{p}\gamma + \bar{N}(1440)p\gamma$ model with the Np form factor reproducing the experimental $p\bar{p}\pi^0$ mass distribution. In the simulation, the ratio of detection efficiencies for the $p\bar{p}\gamma$ and $p\bar{p}\pi^0\gamma$ selection criteria is $(1.5 \pm 0.2)\%$. From 847 ± 31 selected $e^+e^- \to p\bar{p}\pi^0\gamma$ candidates (Fig. 8) the background contribution to the sample of $e^+e^- \to p\bar{p}\gamma$ candidates is estimated to be 13 ± 3 events (about 0.3% of the total number of selected $p\bar{p}\gamma$ candidates).

The background contribution from ISR processes with higher multiplicity is significantly lower. A procedure similar to that described above is used to estimate the background from the $e^+e^- \to p\bar{p}2\pi^0\gamma$ process. Performing a kinematic fit under the $e^+e^- \to p\bar{p}2\pi^0\gamma$ hypothesis, 560 ± 30 events are selected. From the Monte-Carlo simulation, the ratio of detection efficiencies for the $p\bar{p}\gamma$ and $p\bar{p}2\pi^0\gamma$ selection criteria is $(0.09 \pm 0.06)\%$, and the background contribution due to $e^+e^- \to p\bar{p}2\pi^0\gamma$ is estimated to be 0.5 ± 0.3 events.

D. Background subtraction

Table III summarizes the expected number of background events estimated in the above sections. The *uds* column shows the number of background events expected from $e^+e^- \to q\bar{q}$ with the $p\bar{p}\pi^0$ final state excluded. This background is estimated using the JETSET event generator. Because JETSET has not been precisely verified for the rare processes contributing to the $p\bar{p}\gamma$ candidate sample, the background estimation is based on the difference in χ^2 distributions for signal and background events. The second row in Table III lists β_i, the ratio of N_2, the number of events with $30 < \chi^2_p < 60$, to N_1, the number of events with $\chi^2_p < 30$, calculated for signal and background processes using the Monte-Carlo simulation. The last row in Table III shows the expected numbers of signal and background events in the χ^2 sideband ($30 < \chi^2_p < 60$) calculated as $N_2 = \beta N_1$. In the Table, it is evident that χ^2 distributions for signal events and those for background from the processes with higher hadron multiplicity (columns labeled *uds* and $p\bar{p}\pi^0\gamma$) are very different. This difference can be used to estimate the background from these two sources, as follows. First, the $\pi^+\pi^-\gamma$, $K^+K^-\gamma$, $e^+e^-\gamma$, and $p\bar{p}\pi^0$ background determined in previous sections is subtracted from data. Then, from the resulting numbers of events in the signal and sideband χ^2 regions, N'_1 and N'_2, the numbers of signal and background (from *uds* and $p\bar{p}\pi^0\gamma$ sources) events with $\chi^2_p < 30$ can be calculated:

TABLE III. N_1 and N_2 are the numbers of selected $p\bar{p}\gamma$ candidates with a kinematic fit $\chi^2_p < 30$ and $30 < \chi^2_p < 60$, respectively, for signal and for different background processes. The last column shows the numbers of candidates selected in data. β_i is the ratio N_2/N_1 obtained from simulation. The numbers for $e^+e^- \to p\bar{p}\gamma$ are obtained from data using the background subtraction procedure described in the text.

	$\pi^+\pi^-\gamma$	$K^+K^-\gamma$	$p\bar{p}\pi^0$	$p\bar{p}\pi^0\gamma$	*uds*	$p\bar{p}\gamma$	data
N_1	5.9 ± 2.5	2.5 ± 1.0	229 ± 32	13 ± 3	26 ± 4	3737 ± 75	4025
β_i	0.71 ± 0.05	0.52 ± 0.04	0.13 ± 0.01	1.53 ± 0.25	1.44 ± 0.30	0.048 ± 0.001	$\cdots$
N_2	4.2 ± 1.8	1.3 ± 0.5	29 ± 5	20 ± 3	37 ± 5	179 ± 5	288

$$N_{\rm sig} = \frac{N_1' - N_2'/\beta_{\rm bkg}}{1 - \beta_{p\bar{p}\gamma}/\beta_{\rm bkg}}, \qquad N_{\rm bkg} = N_1' - N_{\rm sig}, \qquad (4)$$

where $\beta_{\rm bkg}$ is the ratio of fractions of events in the sideband and signal χ^2 regions averaged over uds and $p\bar{p}\pi^0\gamma$ backgrounds. For this coefficient $\beta_{\rm bkg} = 1.5 \pm 0.4$ is used; it is the average of β_{uds} and $\beta_{p\bar{p}\pi^0\gamma}$ with an uncertainty covering the full range of β_{uds} and $\beta_{p\bar{p}\pi^0\gamma}$ variations.

In Table III, it is also evident that $p\bar{p}\gamma$ events dominate the sideband. Therefore, the background is very sensitive to the accuracy of the $\beta_{p\bar{p}\gamma}$ coefficient. In particular, the data-Monte-Carlo difference in the χ^2 distribution can lead to a systematic shift of the result. The simulation of the χ^2 distribution for $p\bar{p}\gamma$ events is validated using data and simulated events in the channels $e^+e^- \to \mu^+\mu^-\gamma$ and $e^+e^- \to K^+K^-\gamma$, both of which are kinematically very similar to the process under study. In the simulations, the β coefficients for all three processes agree within 2%. The ratio of the β coefficients for data and simulation is 1.01 ± 0.03 for $e^+e^- \to K^+K^-\gamma$ and 1.015 ± 0.012 for $e^+e^- \to \mu^+\mu^-\gamma$. The $\mu^+\mu^-\gamma$ ratio is used to correct the $\beta_{p\bar{p}\gamma}$ value obtained from simulation, which results in $\beta_{p\bar{p}\gamma} = 0.048 \pm 0.003$. The error is estimated using the $\beta_{p\bar{p}\gamma}$ variation as a function of $p\bar{p}$ mass.

With the method described above, the total number of $e^+e^- \to p\bar{p}\gamma$ events ($N_{\rm sig}$) and background events from uds and $p\bar{p}\pi^0\gamma$ sources ($N_{\rm bkg}$) in the signal region are $3737 \pm 67 \pm 34$ and $50 \pm 12 \pm 16$, respectively. The main source of the systematic uncertainty on $N_{\rm sig}$ is the uncertainty in the $p\bar{p}\pi^0$ background. The numbers of uds and $p\bar{p}\pi^0\gamma$ background events are in good agreement with their estimations from simulation, $(13 \pm 3) + (26 \pm 4) = 39 \pm 5$. The total background in the $\chi^2_p < 30$ region is 288 events, about 8% of the number of signal events.

The background subtraction procedure is performed in each $p\bar{p}$ mass bin. The resulting numbers of signal events for each bin are listed in Table VI. The events from J/ψ and $\psi(2S)$ decays are subtracted from the contents of the corresponding bins (see Sec. VIII).

V. ANGULAR DISTRIBUTION

The ratio of electric and magnetic form factors is extracted by analyzing the distribution of θ_p, the angle between the proton momentum in the $p\bar{p}$ rest frame and the momentum of the $p\bar{p}$ system in the e^+e^- center-of-mass frame. In general, this distribution is given by

$$\frac{{\rm d}N}{{\rm d}\cos\theta_p} = A\Big(H_M(\cos\theta_p, M_{p\bar{p}}) + \left|\frac{G_E}{G_M}\right|^2 H_E(\cos\theta_p, M_{p\bar{p}})\Big). \qquad (5)$$

The functions $H_M(\cos\theta_p, M_{p\bar{p}})$ and $H_E(\cos\theta_p, M_{p\bar{p}})$ do not have simple analytic forms, but are determined using MC simulation. Two samples of $e^+e^- \to p\bar{p}\gamma$ events are generated, one with $G_E = 0$ and the other with $G_M = 0$. The obtained functions are similar to the $1 + \cos^2\theta_p$ and $\sin^2\theta_p$ functions describing angular distributions for magnetic and electric form factors in the case of the $e^+e^- \to p\bar{p}$ process.

The angular distributions of the data are fit in six ranges of $p\bar{p}$ invariant mass from threshold to 3 GeV/c^2 to measure $|G_E/G_M|$. The fit intervals, the corresponding numbers of selected events, and the estimated numbers of background events are listed in Table IV. For each $p\bar{p}$ mass interval and each angular bin the background is subtracted using the procedure described in Sec. IV D. The angular distributions obtained are shown in Fig. 9. The distributions are fit to Eq. (5) with two free parameters A (the overall normalization) and $|G_E/G_M|$. The functions H_M and H_E are modeled with the histograms obtained from MC simulation with the $p\bar{p}\gamma$ selection applied. To account for differences between the $p\bar{p}$ mass distributions of $p\bar{p}\gamma$ events in data and MC simulation, the histograms H_M and H_E are recalculated using weighted events. The weights are obtained from the ratio of the $p\bar{p}$ mass distributions in data and simulation. In principle, the weights for H_M and H_E differ due to the different mass dependences of G_M and G_E. A first approximation uses $G_M = G_E$. The fitted values of $|G_E/G_M|$ are then used in the next approximation to recalculate H_M and H_E. The second iteration leads to a small change (less than 2%) of the fitted values, and the procedure converges after a third iteration.

The simulated angular distributions are corrected to account for the differences between the data and the simulations, in particle identification, tracking, and photon efficiencies. These corrections are discussed in detail in the next section. The angular dependences of detection efficiencies calculated with MC simulation before and after corrections are shown in Fig. 10. The variations from uniform, which do not exceed 10% fractionally, derive from the momentum dependences of proton/antiproton particle identification efficiencies. These manifest themselves as angular variations because there is a strong correlation between proton/antiproton momentum and θ_p. In particular, the minima in detection efficiency at $|\cos\theta_p| = 0.75$ correspond to the minima in proton/anti-

TABLE IV. N is the number of selected $p\bar{p}\gamma$ candidates, $N_{\rm bkg}$ is the number of background events, and $|G_E/G_M|$ is the fitted ratio of form factors, for each $p\bar{p}$ mass interval.

$M_{p\bar{p}}$, GeV/c^2	N	$N_{\rm bkg}$	$\lvert G_E/G_M\rvert$
1.877–1.950	533	2 ± 7	$1.41^{+0.24+0.17}_{-0.22-0.12}$
1.950–2.025	584	37 ± 12	$1.78^{+0.31+0.18}_{-0.25-0.14}$
2.025–2.100	602	50 ± 15	$1.52^{+0.27+0.16}_{-0.23-0.12}$
2.100–2.200	705	42 ± 14	$1.18^{+0.20+0.12}_{-0.19-0.11}$
2.200–2.400	592	61 ± 16	$1.32^{+0.26+0.17}_{-0.23-0.14}$
2.400–3.000	464	45 ± 12	$1.22^{+0.30+0.16}_{-0.30-0.16}$

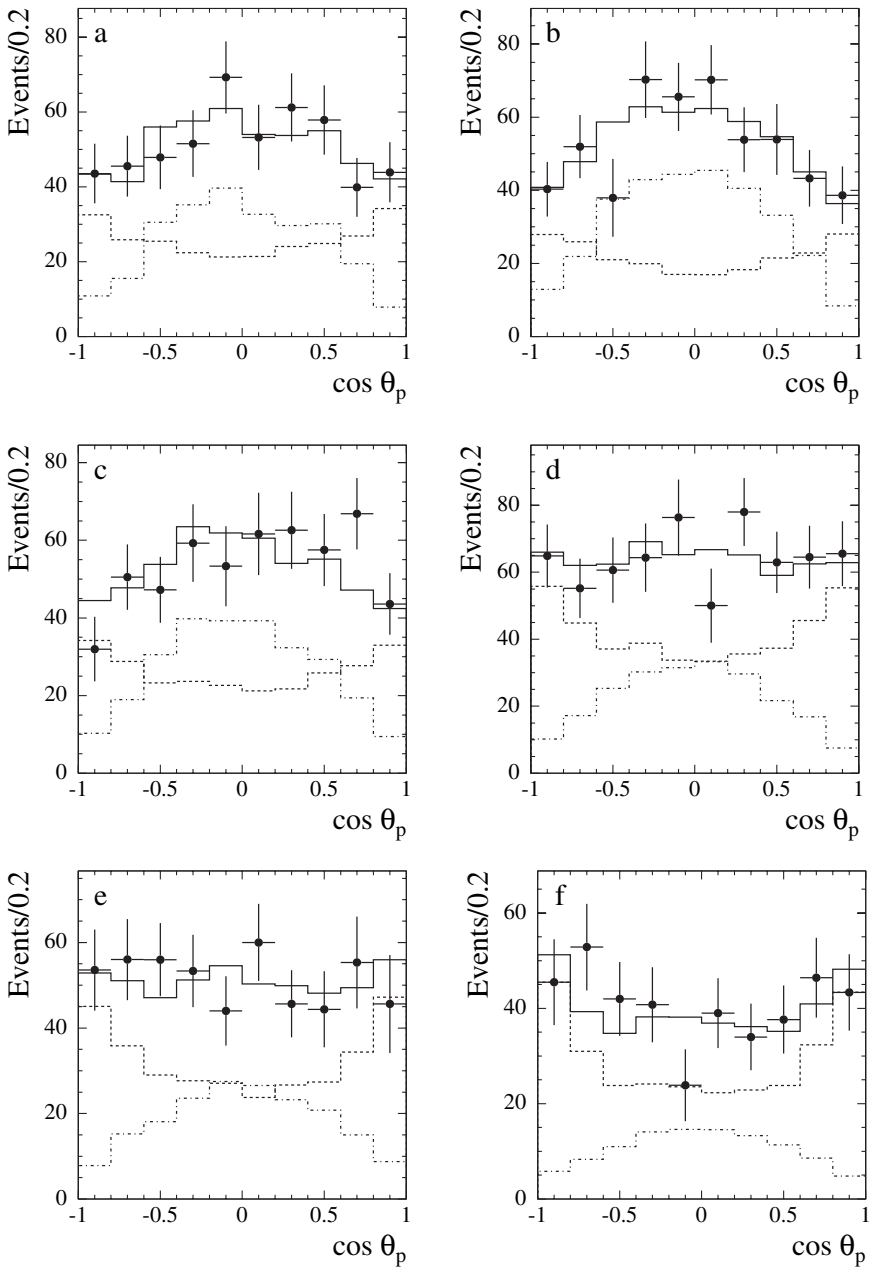

FIG. 9. The $\cos\theta_p$ distributions for different $p\bar{p}$ mass regions: (a) 1.877–1.950 GeV/c^2, (b) 1.950–2.025 GeV/c^2, (c) 2.025–2.100 GeV/c^2, (d) 2.100–2.200 GeV/c^2, (e) 2.200–2.400 GeV/c^2, (f) 2.400–3.000 GeV/c^2. The points with error bars show data distributions after background subtraction. The histograms are fit results: the dashed histograms show the contributions corresponding to the magnetic form factor; the dash-dotted histograms show the contributions from the electric form factor.

proton identification efficiencies for momenta near 1.5 GeV/c.

The histograms fit to the angular distributions are shown in Fig. 9; the values of $|G_E/G_M|$ are listed in Table IV and shown in Fig. 11. The curve in Fig. 11 $[1 + ax/(1 + bx^2)]$ is used in the iteration procedure to calculate the weight. The quoted errors on $|G_E/G_M|$ are statistical and systematic. The dominant contribution to the systematic error comes from the uncertainty in the $p\bar{p}\pi^0$ background. For example, for the 1.950–2.025 GeV/c^2 range this contribution to the lower (upper) error is 0.12 (0.16), which dominates the total systematic error in this bin, and likewise dominates systematic error in all bins. The error due to the limited MC simulation statistics (0.08 for 1.950–2.025 GeV/c^2), uncertainties in the coefficients β used for background subtraction (0.01), the uncertainty of description of mass dependence of $|G_E/G_M|$ (0.01), and the uncertainty in the efficiency correction (0.02) are all

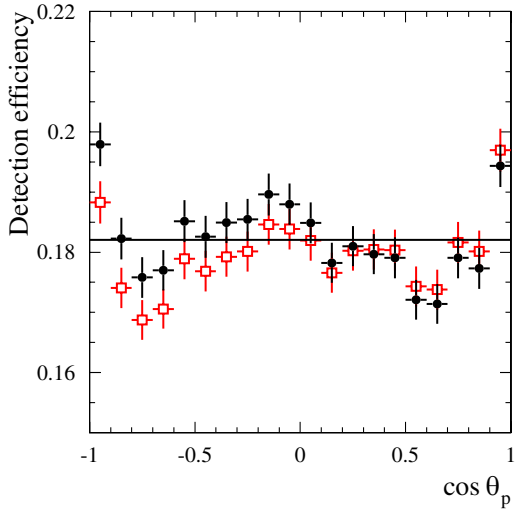

FIG. 10 (color online). The angular dependence of the detection efficiency for simulated events with $M_{p\bar{p}} < 2.5$ GeV/c^2 before (open squares) and after (filled circles) correction for data-simulation difference in detector response.

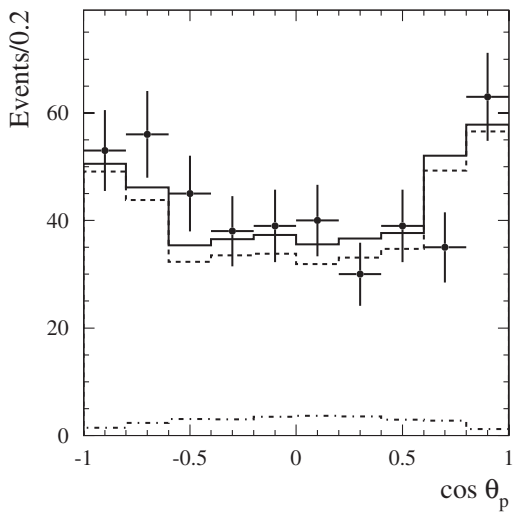

FIG. 12. The $\cos\theta_p$ distributions for $J/\psi \to p\bar{p}$ decay. The points with error bars correspond to the background-subtracted data distribution, the solid histogram is the fit result, and the dashed and dashed-dotted histograms show the fit contributions from the magnetic and electric form factors, respectively.

considered. The last is conservatively estimated as the difference between fitted values of $|G_E/G_M|$ obtained with and without applying the efficiency correction.

The angular distribution for $J/\psi \to p\bar{p}$ decay has also been studied. Its shape is commonly parametrized using the form $1 + \alpha\cos^2\vartheta$. The coefficient α has been measured with relatively high precision in several experiments [21,22], and its average value is $\alpha = 0.660 \pm 0.045$. The *BABAR* data distribution for $J/\psi \to p\bar{p}$ decay is shown in Fig. 12. The nonpeaking background is subtracted by taking the difference between the histograms for the signal mass region (3.05–3.15 GeV/c^2) and the mass sidebands (3.00–3.05 and 3.15–3.20 GeV/c^2). The fitting procedure used is similar to the one described above with $\alpha = (1 - g\tau)/(1 + g\tau)$, where $g = |G_E/G_M|^2$ and $\tau = 4m_p^2/M_{J/\psi}^2$. The resulting value $\alpha = 0.75^{+0.42}_{-0.35}$ is in agreement with the world average but has significantly larger uncertainty.

To cross-check this method to measure $|G_E/G_M|$, a comparison is made between the data and simulated distributions of $\cos\theta_K$ for the $e^+e^- \to \phi\gamma \to K^+K^-\gamma$ process. Here θ_K is defined analogous to the definition of θ_p: θ_K is the angle between the K^- momentum in the K^+K^- rest frame and the momentum of the K^+K^- system in the e^+e^- center-of-mass frame. The angular dependence for

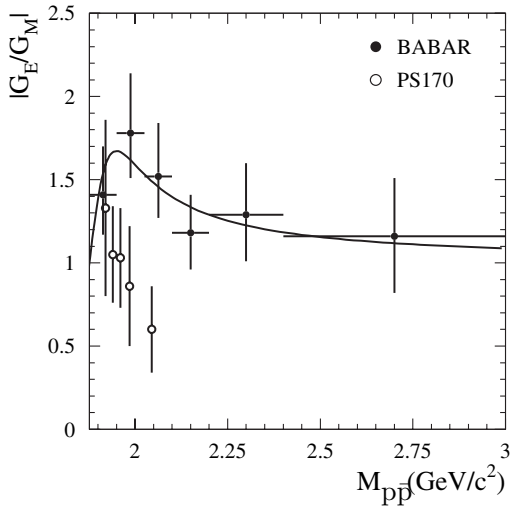

FIG. 11. The measured $|G_E/G_M|$ mass dependence. Filled circles depict *BABAR* data; the curve is the fit result. Open circles show the data from PS170 [10].

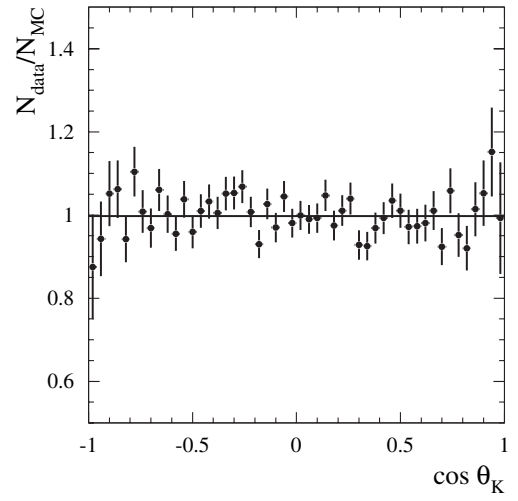

FIG. 13. The ratio of data and simulated distributions of $\cos\theta_K$ for the $e^+e^- \to K^+K^-\gamma$ process.

this process is well known (approximately $\cos^2\theta_K$) and event kinematics are similar to the $e^+e^- \to p\bar{p}\gamma$ kinematics near threshold. Figure 13 shows the ratio of data and simulated distributions over $\cos\theta_K$ for events with the K^+K^- mass near the ϕ. The simulation describes the angular dependence of detection efficiency well.

When these *BABAR* measurements of the $|G_E/G_M|$ ratio are compared with the PS170 measurements [10] (Fig. 11), a large disagreement is seen for $M_{p\bar{p}}$ larger than 1.93 GeV/c^2.

VI. DETECTION EFFICIENCY

The detection efficiency, determined using Monte-Carlo simulation, is the ratio of true $p\bar{p}$ mass distributions computed after and before applying selection criteria. Because the $e^+e^- \to p\bar{p}\gamma$ differential cross section depends on the form factors, the detection efficiency is somewhat model dependent. The model used in this study has the $|G_E/G_M|$ ratio obtained from a fit of experimental angular distributions (curve in Fig. 11) for $M_{p\bar{p}} < 3$ GeV/c^2, and $|G_E/G_M| = 1$ for higher masses. The detection efficiency calculated in this model, shown in Fig. 14, is fit to a third-order polynomial for $M_{p\bar{p}} < 3$ GeV/c^2 and a constant for $M_{p\bar{p}} > 3$ GeV/c^2. The statistical error of the detection efficiency is about 1%. The model error is determined from the uncertainty in the $|G_E/G_M|$ ratio: for $M_{p\bar{p}} < 3$ GeV/c^2, varying the ratio within its experimental uncertainty leads to a 1% change in the detection efficiency. This is taken as the model error. This small value is not surprising, due to the relatively small difference between the detector sensitivities for pure electric and magnetic transitions. This difference was calculated with simulated event samples in which $G_E = 0$ and $G_M = 0$ and is shown as a function of $M_{p\bar{p}}$ in Fig. 15. It does not exceed 20%. For masses above 3 GeV/c^2, where the $|G_E/G_M|$ ratio is unknown, a 10% model error equal to half of the difference between detection efficiencies corresponding to $G_M = 0$ and $G_E = 0$ is used.

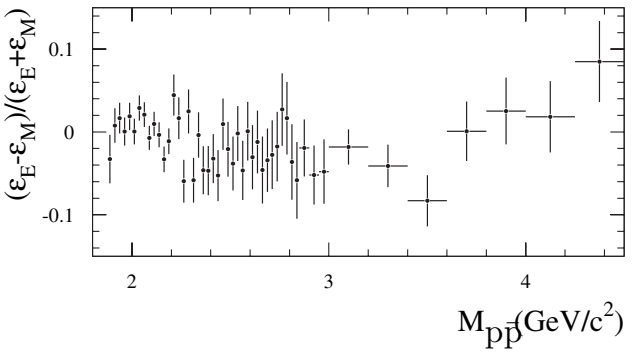

FIG. 15. The relative difference between detection efficiencies for a purely electric ($G_M = 0$) and purely magnetic ($G_E = 0$) transition in the $e^+e^- \to p\bar{p}\gamma$ reaction.

The efficiency determined from MC simulation ($\varepsilon_{\rm MC}$) must be corrected to account for data-MC simulation differences in detector response:

$$\varepsilon = \varepsilon_{\rm MC} \prod (1 + \delta_i), \tag{6}$$

where δ_i are efficiency corrections for each of several effects. These corrections are discussed in detail below and summarized in Table V.

Inaccuracy in the simulation of angular and momentum resolutions and radiative corrections may account for some of the data-MC difference in the fraction of events rejected by the requirement that $\chi^2_p < 30$. The efficiency correction for this effect is estimated by comparing data and simulated χ^2 distributions for the $e^+e^- \to \mu^+\mu^-\gamma$ process, which has kinematics similar to the process under study. An exclusive $e^+e^- \to \mu^+\mu^-\gamma$ sample is selected by requiring that both charged tracks be identified as muons. To remove possible background contributions from hadronic events with $J/\psi \to \mu^+\mu^-$ decay, events with di-muon invariant mass in the range $3.0 < M_{\mu\mu} < 3.2$ GeV/c^2 are excluded. The ratio of the number of selected muon events with $\chi^2_\mu > 30$ and $\chi^2_\mu < 30$ varies from 0.35 to 0.4 in the

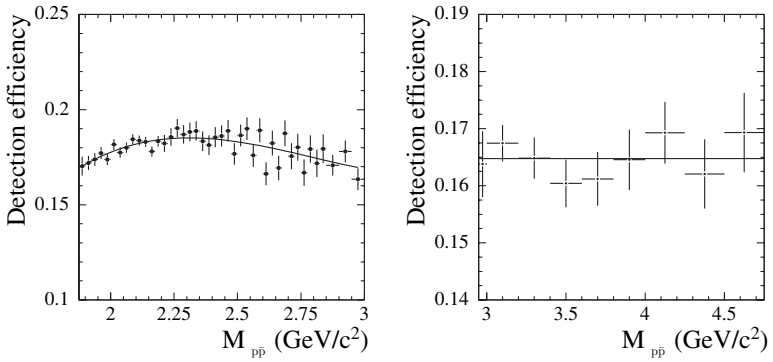

FIG. 14. The $p\bar{p}$ mass dependence of detection efficiency obtained from MC simulation. The line on the left plot is the fit to a third-order polynomial. The efficiency for $M_{p\bar{p}} > 3$ GeV/c^2 is fit to a constant value.

TABLE V. The values of different efficiency corrections δ_i for $p\bar{p}$ masses 1.9, 3.0, and 4.5 GeV/c^2.

Effect	$\delta_i(1.9)$, %	$\delta_i(3)$, %	$\delta_i(4.5)$, %
$\chi^2_p < 30$ cut	-0.7 ± 1.0	-1.1 ± 1.0	-1.7 ± 1.0
$\chi^2_K > 30$ cut	0.0 ± 0.7	0.0 ± 0.7	0.0 ± 0.7
Track reconstruction	0.0 ± 3.0	0.0 ± 3.0	0.0 ± 3.0
Nuclear interaction	0.8 ± 0.4	1.1 ± 0.4	1.0 ± 0.4
PID	2.5 ± 3.3	3.2 ± 2.4	3.5 ± 2.7
Photon inefficiency	-1.3 ± 0.1	-1.3 ± 0.1	-1.3 ± 0.1
Photon conversion	0.4 ± 0.2	0.4 ± 0.2	0.4 ± 0.2
Trigger	-0.6 ± 0.3	...	...
Total	1.1 ± 4.7	2.3 ± 4.1	1.9 ± 4.2

$M_{p\bar{p}}$ range from threshold to 4.5 GeV/c^2. When comparing data and MC simulation in the region $\chi^2_\mu > 30$, the cut $M_{\mu\mu\gamma} < 8$ GeV/c^2 needs to be applied, for consistency, to the data sample, since this cut is already applied to the MC simulation and therefore some events of this nonsignal region are rejected in the simulated sample. To characterize data-MC simulation difference in the χ^2 distribution, a double ratio (κ) is calculated as the ratio of $N(\chi^2_\mu > 30)/N(\chi^2_\mu < 30)$ obtained from data to the same quantity obtained from MC simulation. The value of the double ratio is $\kappa = 1.04 \pm 0.01$, essentially independent of mass. The efficiency correction for the χ^2 cut is calculated as

$$\delta_1 = \frac{N(\chi^2 < 30) + N(\chi^2 > 30)}{N(\chi^2 < 30) + \kappa N(\chi^2 > 30)} - 1, \qquad (7)$$

where $N(\chi^2 < 30)$ and $N(\chi^2 > 30)$ are the numbers of simulated $p\bar{p}\gamma$ events with $\chi^2 < 30$ and $\chi^2 > 30$, respectively. The values of the efficiency correction δ_1 for different $p\bar{p}$ masses are listed in Table V. Its statistical error is about 0.3%. An additional 1% systematic error, equal to the correction variation in the $p\bar{p}$ mass region of interest, is added in quadrature.

The effect of the $\chi^2_K > 30$ cut is studied using $e^+e^- \to J/\psi\gamma \to p\bar{p}\gamma$ events. The number of J/ψ's is determined using the sideband subtraction method. The event losses due to the $\chi^2_K > 30$ cut are found to be $1.7 \pm 0.7\%$ in data and $1.7 \pm 0.2\%$ in MC simulation. As the data and simulated values are in good agreement, there is no need to introduce any efficiency corrections for the $\chi^2_K > 30$ cut. The systematic uncertainty associated with this cut is 0.7%.

Another possible source of data-MC simulation differences is track loss. The systematic uncertainty due to differences in track reconstruction is estimated to be 1.3% per track. Specifically, for $e^+e^- \to p\bar{p}\gamma$ only, the systematic error can originate from slightly imperfect simulation of nuclear interactions of protons and antiprotons in the material before the SVT and DCH. The simulation shows that nuclear interaction leads to the loss of approximately 6% of $e^+e^- \to p\bar{p}\gamma$ events. For data-MC simulation comparison, a specially selected event sample with $\Lambda(\bar{\Lambda})$ decaying into $p(\bar{p})\pi$ is used. The Λ are selected by imposing requirements on $p\pi$ invariant mass and the Λ flight distance. The amount of material before the SVT (1.5% of nuclear interaction length) is comparable to the amount of material between the SVT and the DCH (1.4% of nuclear interaction length). The probability of track losses between the SVT and the DCH is measured from the $\Lambda(\bar{\Lambda})$ sample. The data and simulation probabilities are found to be in good agreement for protons. A substantial difference is observed for antiprotons, which is consistent with a large (a factor of 2.6 ± 1.0) overestimation of the antiproton annihilation cross section in simulation. This difference in the antiproton annihilation cross section in data and simulation leads to a correction of about $(1.0 \pm 0.4)\%$ to the detection efficiency for $p\bar{p}\gamma$ events.

The data-MC simulation difference in the particle identification is studied with use of events with a $J/\psi \to p\bar{p}$ decay. Because of the narrow J/ψ width and low background, the number of $J/\psi \to p\bar{p}$ decays may be determined using selections with either one or two identified protons. The background from non-J/ψ events is subtracted using sidebands. The $p/\bar{p}$ identification probabilities are determined as functions of the $p/\bar{p}$ momenta by calculating the ratio of the number of events with both the proton and the antiproton identified to the number of events with only one identified proton or antiproton. The ratio of data-MC identification probabilities is used to reweight selected simulated events and calculate efficiency corrections. The correction is about $(3 \pm 3)\%$ and varies within 0.5% depending on the $p\bar{p}$ mass. The error in the correction factor is determined from the statistical uncertainty in the number of selected J/ψ events.

Another correction must be applied to the photon detection efficiency. There are two main sources for this correction: data-MC simulation differences in the probability of photon conversion in the detector material before the DCH, and the effect of dead calorimeter channels. A sample of $e^+e^- \to \mu^+\mu^-\gamma$ events is used to determine the photon inefficiency in data. Events with exactly two oppositely charged tracks identified as muons are selected and a kinematic fit is performed, constraining zero recoil mass against the muon pair. A tight cut on χ^2 of the kinematic fit selects events with only one photon in the final state. The photon direction is determined from the fit. The photon detection inefficiency is calculated using the ratio of the number of events not passing the $E^*_\gamma > 3$ GeV cut to the total number of selected $\mu^+\mu^-\gamma$ events. The obtained 3.3% photon inefficiency can be compared to the 2% inefficiency in $e^+e^- \to p\bar{p}\gamma$ simulation. The observed data-MC difference in the photon inefficiency leads to an efficiency correction of $(-1.3 \pm 0.1)\%$ that is practically independent of the $p\bar{p}$ mass. The data-MC simulation difference in the probability of photon conversion is studied using $e^+e^- \to \gamma\gamma$ events and found to be $(0.4 \pm 0.2)\%$.

The quality of the simulation of the trigger efficiency is also studied. The overlap of the samples of events passing different trigger criteria and the independence of these triggers are used to measure the trigger efficiency. A small difference $[(-0.6 \pm 0.3)\%]$ in trigger efficiency between data and MC simulation is observed for $p\bar{p}$ masses below 2.025 GeV/c^2.

All efficiency corrections are summarized in Table V. The corrected detection efficiencies are listed in Table VI. The uncertainty in detection efficiency includes a simulation statistical error, a model uncertainty, and the uncertainty of the efficiency correction.

VII. $e^+e^- \to p\bar{p}$ CROSS SECTION AND PROTON FORM FACTOR

The cross section for $e^+e^- \to p\bar{p}$ is calculated from the $p\bar{p}$ mass spectrum using the expression

$$\sigma_{p\bar{p}}(m) = \frac{(\mathrm{d}N/\mathrm{d}m)_{\mathrm{corr}}}{\varepsilon R \mathrm{d}L/\mathrm{d}m}, \tag{8}$$

TABLE VI. The $p\bar{p}$ invariant mass ($M_{p\bar{p}}$), the number of selected events (N) after background subtraction, detection efficiency (ε), the ISR luminosity (L), the measured cross section ($\sigma_{p\bar{p}}$), and F_p, the effective form factor for $e^+e^- \to p\bar{p}$. The contribution of $J/\psi \to p\bar{p}$ and $\psi(2S) \to p\bar{p}$ decays has been subtracted. The quoted uncertainties in N and σ are statistical and systematic. For the form factor, the combined uncertainty is listed.

$M_{p\bar{p}}$ (GeV/c^2)	N	ε	L (pb^{-1})	$\sigma_{p\bar{p}}$ (pb)	$\lvert F_p \rvert$
1.877–1.900	$157 \pm 13 \pm 3$	0.171 ± 0.008	1.141	$802 \pm 68 \pm 43$	$0.453^{+0.023}_{-0.025}$
1.900–1.925	$190 \pm 15 \pm 3$	0.173 ± 0.008	1.236	$887 \pm 71 \pm 46$	$0.354^{+0.017}_{-0.017}$
1.925–1.950	$180 \pm 15 \pm 3$	0.175 ± 0.008	1.254	$819 \pm 68 \pm 43$	$0.305^{+0.015}_{-0.015}$
1.950–1.975	$171 \pm 15 \pm 4$	0.177 ± 0.008	1.272	$760 \pm 68 \pm 41$	$0.276^{+0.014}_{-0.015}$
1.975–2.000	$176 \pm 16 \pm 5$	0.178 ± 0.008	1.290	$765 \pm 68 \pm 44$	$0.266^{+0.014}_{-0.015}$
2.000–2.025	$201 \pm 17 \pm 5$	0.180 ± 0.008	1.308	$854 \pm 71 \pm 48$	$0.273^{+0.013}_{-0.014}$
2.025–2.050	$181 \pm 16 \pm 6$	0.182 ± 0.008	1.328	$748 \pm 68 \pm 45$	$0.250^{+0.013}_{-0.014}$
2.050–2.075	$196 \pm 17 \pm 6$	0.183 ± 0.008	1.346	$794 \pm 68 \pm 46$	$0.254^{+0.013}_{-0.014}$
2.075–2.100	$180 \pm 17 \pm 5$	0.184 ± 0.008	1.365	$715 \pm 66 \pm 40$	$0.239^{+0.013}_{-0.013}$
2.100–2.125	$203 \pm 18 \pm 5$	0.185 ± 0.008	1.383	$794 \pm 68 \pm 44$	$0.250^{+0.012}_{-0.013}$
2.125–2.150	$188 \pm 17 \pm 5$	0.185 ± 0.009	1.402	$721 \pm 66 \pm 40$	$0.237^{+0.012}_{-0.013}$
2.150–2.175	$147 \pm 15 \pm 5$	0.186 ± 0.009	1.421	$554 \pm 58 \pm 34$	$0.207^{+0.012}_{-0.013}$
2.175–2.200	$128 \pm 15 \pm 6$	0.187 ± 0.009	1.440	$477 \pm 56 \pm 31$	$0.191^{+0.012}_{-0.013}$
2.200–2.225	$119 \pm 14 \pm 5$	0.187 ± 0.009	1.459	$435 \pm 52 \pm 29$	$0.183^{+0.012}_{-0.013}$
2.225–2.250	$109 \pm 13 \pm 3$	0.187 ± 0.009	1.478	$392 \pm 47 \pm 21$	$0.174^{+0.011}_{-0.012}$
2.250–2.275	$69 \pm 11 \pm 3$	0.188 ± 0.008	1.497	$245 \pm 40 \pm 16$	$0.137^{+0.012}_{-0.013}$
2.275–2.300	$70 \pm 11 \pm 5$	0.188 ± 0.008	1.516	$244 \pm 39 \pm 20$	$0.137^{+0.012}_{-0.013}$
2.300–2.350	$82 \pm 12 \pm 9$	0.188 ± 0.008	3.092	$140 \pm 21 \pm 16$	$0.105^{+0.009}_{-0.010}$
2.350–2.400	$80 \pm 11 \pm 7$	0.188 ± 0.008	3.172	$133 \pm 19 \pm 13$	$0.103^{+0.008}_{-0.009}$
2.400–2.450	$91 \pm 11 \pm 2$	0.187 ± 0.008	3.251	$149 \pm 18 \pm 7$	$0.110^{+0.007}_{-0.008}$
2.450–2.500	$52 \pm 9 \pm 2$	0.187 ± 0.008	3.331	$83 \pm 15 \pm 5$	$0.083^{+0.008}_{-0.008}$
2.500–2.550	$63 \pm 10 \pm 2$	0.186 ± 0.008	3.414	$100 \pm 16 \pm 6$	$0.092^{+0.007}_{-0.008}$
2.550–2.600	$39 \pm 8 \pm 2$	0.185 ± 0.008	3.496	$60 \pm 13 \pm 4$	$0.072^{+0.007}_{-0.008}$
2.600–2.650	$31 \pm 8 \pm 2$	0.183 ± 0.008	3.580	$47 \pm 11 \pm 4$	$0.065^{+0.008}_{-0.009}$
2.650–2.700	$25 \pm 7 \pm 2$	0.182 ± 0.008	3.664	$37 \pm 10 \pm 4$	$0.059^{+0.008}_{-0.009}$
2.700–2.750	$21 \pm 7 \pm 2$	0.180 ± 0.008	3.749	$31 \pm 10 \pm 4$	$0.054^{+0.008}_{-0.010}$
2.750–2.800	$25 \pm 7 \pm 2$	0.179 ± 0.008	3.837	$37 \pm 10 \pm 4$	$0.060^{+0.008}_{-0.010}$
2.800–2.850	$20 \pm 6 \pm 2$	0.178 ± 0.008	3.924	$30 \pm 9 \pm 3$	$0.054^{+0.008}_{-0.009}$
2.850–2.900	$19 \pm 6 \pm 2$	0.176 ± 0.008	4.013	$27 \pm 9 \pm 3$	$0.052^{+0.008}_{-0.010}$
2.900–2.950	$19 \pm 6 \pm 2$	0.175 ± 0.007	4.103	$26 \pm 8 \pm 3$	$0.052^{+0.008}_{-0.009}$
2.950–3.000	$9 \pm 5 \pm 2$	0.173 ± 0.007	4.195	$12 \pm 7 \pm 3$	$0.035^{+0.010}_{-0.014}$
3.000–3.200	$11 \pm 9 \pm 8$	0.169 ± 0.018	17.719	$3.6 \pm 3.0 \pm 2.8$	$0.021^{+0.009}_{-0.021}$
3.200–3.400	$8 \pm 5 \pm 7$	0.169 ± 0.018	19.289	$2.3 \pm 1.6 \pm 2.0$	$0.017^{+0.008}_{-0.017}$
3.400–3.600	$6 \pm 4 \pm 3$	0.169 ± 0.018	20.960	$1.7 \pm 1.0 \pm 0.9$	$0.016^{+0.005}_{-0.009}$
3.600–3.800	$8 \pm 4 \pm 3$	0.168 ± 0.018	22.739	$2.2 \pm 1.1 \pm 0.8$	$0.019^{+0.005}_{-0.008}$
3.800–4.000	$5 \pm 3 \pm 3$	0.168 ± 0.018	24.645	$1.2 \pm 0.8 \pm 0.7$	$0.015^{+0.005}_{-0.009}$
4.000–4.250	$4 \pm 3 \pm 3$	0.168 ± 0.018	33.701	$0.7 \pm 0.5 \pm 0.5$	$0.011^{+0.005}_{-0.010}$
4.250–4.500	$1 \pm 3 \pm 3$	0.167 ± 0.018	37.214	$0.1 \pm 0.4 \pm 0.5$	$0.005^{+0.008}_{-0.005}$

where m is the $p\bar{p}$ invariant mass, $(\mathrm{d}N/\mathrm{d}m)_{\mathrm{corr}}$ is the mass spectrum corrected for resolution effects, $\mathrm{d}L/\mathrm{d}m$ is the ISR differential luminosity, ε is the detection efficiency as a function of mass, and R is a radiative-correction factor accounting for the Born mass spectrum distortion due to emission of several photons by the initial electron or positron. The ISR luminosity is calculated using the total integrated luminosity L and the probability density function for ISR photon emission in Eq. (2):

$$\frac{\mathrm{d}L}{\mathrm{d}m} = \frac{\alpha}{\pi x}\left((2-2x+x^2)\log\frac{1+C}{1-C} - x^2 C\right)\frac{2m}{s}L. \quad (9)$$

Here $x = 1 - m^2/s$, $\sqrt{s}$ is the e^+e^- center-of-mass energy, $C = \cos\theta_0^*$, and θ_0^* determines the range of polar angles in the e^+e^- center-of-mass frame: $\theta_0^* < \theta_\gamma^* < 180^\circ - \theta_0^*$ for the ISR photon. In this study, $\theta_0^* = 20^\circ$, because the detector efficiency is determined using a simulation with $20^\circ < \theta_\gamma^* < 160^\circ$. The integrated ISR luminosity for each $M_{p\bar{p}}$ bin is listed in Table VI.

The radiative-correction factor R is determined using Monte-Carlo simulation at the generator level, without any detector simulation. Two $p\bar{p}$ mass spectra are generated; the first using the pure Born amplitude for the process $e^+e^- \to p\bar{p}\gamma$, and the second using a model with higher-order radiative corrections included with the structure function method [16]. The radiative-correction factor R is the ratio of the second spectrum to the first, and varies from 1.002 at the $p\bar{p}$ threshold to 1.02 at 4.5 GeV mass. The value of R depends on the requirement on the invariant mass of the $p\bar{p}\gamma$ system. The R in this study corresponds to the requirement $M_{p\bar{p}\gamma} > 8$ GeV/c^2 imposed in the simulation. The theoretical uncertainty in the radiative-correction calculation with the structure function method does not exceed 1% [16]. To check the theoretical uncertainty, a comparison of the cross sections calculated with the structure function method and the PHOKHARA [3] event generator is performed. The PHOKHARA generator uses formulas with next-to-leading order radiative corrections in the initial state. The uncertainty of the PHOKHARA generator is estimated to be less than 1% [23]. The ratio of $p\bar{p}$ mass spectra obtained with the two generators differs from unity by about 1% and does not contradict estimates of the theoretical uncertainties. The radiative corrections calculated include initial state radiation and the effect of loops at the electron vertex, but do not include corrections for leptonic and hadronic vacuum polarization in the photon propagator. Cross sections obtained with such corrections are sometimes referred to as "dressed" cross sections while those which account fully for higher-order processes are referred to as "bare" cross sections. See Ref. [24] for a more complete discussion.

The resolution-corrected mass spectrum is obtained by unfolding the mass resolution from the measured mass spectrum. Using the MC simulation, the migration matrix A is obtained, representing the probability that an event with true mass $(M_{p\bar{p}}^{\mathrm{true}})$ in bin j is reconstructed in bin i:

$$\left(\frac{\mathrm{d}N}{\mathrm{d}m}\right)_i^{\mathrm{rec}} = \sum_j A_{ij}\left(\frac{\mathrm{d}N}{\mathrm{d}m}\right)_j^{\mathrm{true}}. \quad (10)$$

As the chosen bin width significantly exceeds the mass resolution for all $p\bar{p}$ masses, the migration matrix is nearly diagonal, with the values of diagonal elements ~0.9, and next-to-diagonal ~0.05. We unfold the mass spectrum by applying the inverse of the migration matrix to the measured spectrum. This procedure changes the shape of the mass distribution insignificantly, but increases the errors (by $\approx 20\%$) and their correlations.

The number of events in each mass bin is listed in Table VI. The quoted errors are statistical and systematic (with the systematic errors due to uncertainties in background subtraction). The calculated cross section for $e^+e^- \to p\bar{p}$ is shown in Fig. 16 and listed in Table VI. For mass bins 3–3.2 GeV/c^2 and 3.6–3.8 GeV/c^2, the nonresonant cross section is quoted with J/ψ and $\psi(2S)$ contributions excluded (see Sec. VIII). The errors quoted are statistical and systematic. The systematic uncertainty includes the uncertainty in the number of signal events and detection efficiency, an error of total integrated luminosity (1%), and the uncertainty in the radiative corrections (1%). A comparison of this result with available e^+e^- data is shown in Fig. 16 and the near-threshold region is shown in Fig. 17.

The $e^+e^- \to p\bar{p}$ cross section is a function of two form factors, but due to poor determination of the $|G_E/G_M|$ ratio, they cannot be extracted from the data simultaneously with reasonable accuracy. Therefore, the effective form factor is introduced:

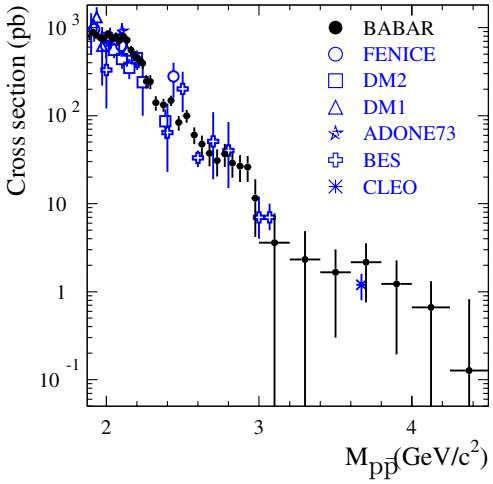

FIG. 16 (color online). The $e^+e^- \to p\bar{p}$ cross section measured in this work and e^+e^- experiments: FENICE [6], DM2 [5], DM1 [4], ADONE73 [7], BES [8], CLEO [9]. The contribution of $J/\psi \to p\bar{p}$ and $\psi(2S) \to p\bar{p}$ decays is subtracted.

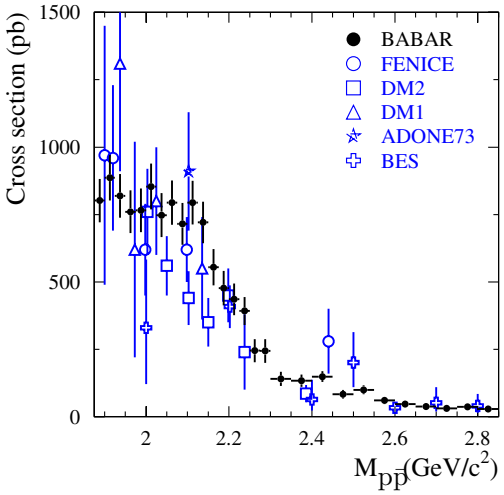

FIG. 17 (color online). The $e^+e^- \to p\bar{p}$ cross section near threshold measured in this work and e^+e^- experiments: FENICE [6], DM2 [5], DM1 [4], ADONE73 [7], BES [8].

$$|F_p(m)| = \sqrt{\sigma_{p\bar{p}}(m)/\sigma_n(m)}, \tag{11}$$

where $\sigma_{p\bar{p}}(m)$ is the measured $e^+e^- \to p\bar{p}$ cross section and $\sigma_n(m)$ is the cross section obtained from Eq. (3) under the assumption that $|G_E| = |G_M| = 1$. At $M_{p\bar{p}} = 2$ GeV/c^2 $\sigma_n \simeq 10$ nb. This definition of the effective form factor $F_p(m)$ permits comparison of our measurements with measurements from other experiments, in e^+e^- as well as $p\bar{p}$ collisions. Most available form-factor data are analyzed using the assumption that $|G_E| = |G_M|$. The calculated effective form factor is shown in Fig. 18 (linear scale), in Fig. 19 (logarithmic scale), and in Table VI. The form factors here are averaged over bin width, and the four points of PS170 [10] with lowest mass are all situated within the first bin of the *BABAR* measurement. For the mass region near threshold where

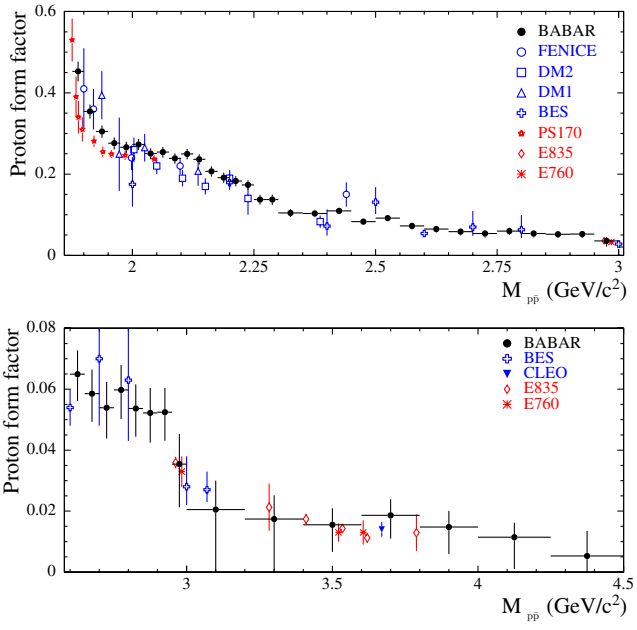

FIG. 18 (color online). The proton effective form factor measured in this work and in e^+e^- and $p\bar{p}$ experiments: FENICE [6], DM2 [5], DM1 [4], BES [8], CLEO [9], PS170 [10], E835 [12], E760 [11]. The upper plot shows the mass interval from the $p\bar{p}$ threshold to 3.01 GeV/c^2. The lower plot presents data for $p\bar{p}$ masses from 2.58 to 4.50 GeV/c^2.

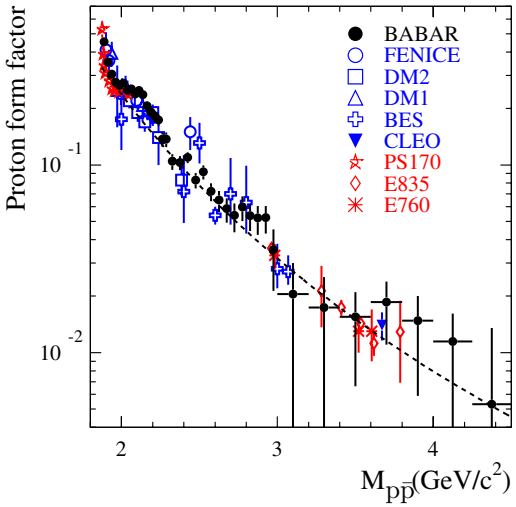

FIG. 19 (color online). The proton effective form factor measured in this work and in e^+e^- and $p\bar{p}$ experiments, shown on a logarithmic scale: FENICE [6], DM2 [5], DM1 [4], BES [8], CLEO [9], PS170 [10], E835 [12], E760 [11]. The curve corresponds to the QCD fit described in the text.

TABLE VII. The $p\bar{p}$ invariant mass ($M_{p\bar{p}}$), the number of selected events (N) after background subtraction, the measured cross section ($\sigma_{p\bar{p}}$), and the effective form factor for $e^+e^- \to p\bar{p}$. The quoted errors in N and $\sigma_{p\bar{p}}$ are statistical and systematic. For the effective form factor, the total combined error is listed.

$M_{p\bar{p}}$ (GeV/c^2)	N	$\sigma_{p\bar{p}}$ (pb)	$\lvert F_p\rvert$
1.8760–1.8800	$18 \pm 5 \pm 1$	$656 \pm 161 \pm 40$	$0.574^{+0.071}_{-0.081}$
1.8800–1.8850	$34 \pm 6 \pm 1$	$808 \pm 155 \pm 43$	$0.495^{+0.047}_{-0.052}$
1.8850–1.8900	$27 \pm 6 \pm 1$	$656 \pm 154 \pm 36$	$0.390^{+0.045}_{-0.050}$
1.8900–1.8950	$37 \pm 7 \pm 1$	$889 \pm 174 \pm 48$	$0.419^{+0.041}_{-0.045}$
1.8950–1.9000	$38 \pm 8 \pm 1$	$901 \pm 182 \pm 48$	$0.398^{+0.040}_{-0.044}$
1.9000–1.9050	$42 \pm 9 \pm 1$	$995 \pm 207 \pm 56$	$0.399^{+0.041}_{-0.046}$
1.9050–1.9100	$31 \pm 8 \pm 1$	$726 \pm 186 \pm 41$	$0.326^{+0.040}_{-0.046}$
1.9100–1.9150	$49 \pm 9 \pm 1$	$1138 \pm 210 \pm 60$	$0.397^{+0.036}_{-0.040}$
1.9150–1.9250	$69 \pm 10 \pm 1$	$798 \pm 116 \pm 43$	$0.321^{+0.024}_{-0.026}$
1.9250–1.9375	$91 \pm 11 \pm 2$	$831 \pm 102 \pm 44$	$0.313^{+0.020}_{-0.022}$
1.9375–1.9500	$90 \pm 11 \pm 2$	$817 \pm 104 \pm 43$	$0.298^{+0.020}_{-0.021}$
1.9500–1.9625	$80 \pm 12 \pm 3$	$712 \pm 105 \pm 42$	$0.270^{+0.021}_{-0.022}$
1.9625–1.9750	$91 \pm 12 \pm 2$	$802 \pm 105 \pm 43$	$0.280^{+0.019}_{-0.020}$

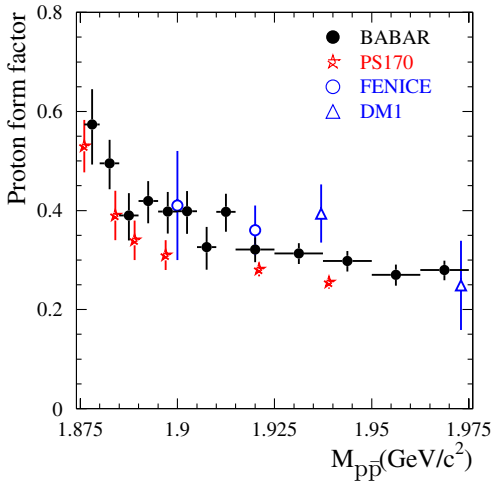

FIG. 20 (color online). The proton effective form factor near the $p\bar{p}$ threshold measured in this work and in e^+e^- and $p\bar{p}$ experiments: FENICE [6], DM1 [4], PS170 [10].

the form factor changes rapidly with mass, the cross section and effective form factor with a smaller bin size are calculated. These results are listed in Table VII. The effective form factor is shown in Fig. 20. In Figs. 18–20, it is evident that the *BABAR* effective form-factor results are in reasonable agreement with those of other experiments. The form factor has a complex mass dependence. The significant increase in form factor as the $p\bar{p}$ threshold is approached may be a manifestation of a $p\bar{p}$ subthreshold resonance [25]. The rapid decreases of the form factor and cross section near 2.25 GeV/c^2 and 3 GeV/c^2 have not been discussed in the literature. The dashed line in Fig. 19 corresponds to the asymptotic QCD fit [26] for proton form factor $F_{p\bar{p}} \sim \alpha_s^2(m^2)/m^4 \sim C/(m^4 \log^2(m^2/\Lambda^2))$, applied to all existing data with $M_{p\bar{p}} > 3$ GeV/c^2. Here $\Lambda = 0.3$ GeV and C is a free fit parameter. It is seen that the asymptotic regime is reached at masses above 3 GeV/c^2.

VIII. THE J/ψ AND $\psi(2S)$ DECAYS INTO $p\bar{p}$

The differential cross section for ISR production of a narrow resonance (vector meson V), such as J/ψ, decaying into the final state f can be calculated using [27]

$$\frac{d\sigma(s, \theta^*_\gamma)}{d\cos\theta^*_\gamma} = \frac{12\pi^2 \Gamma(V \to e^+e^-)\mathcal{B}(V \to f)}{m_V s} W(s, x_V, \theta^*_\gamma), \tag{12}$$

where m_V and $\Gamma(V \to e^+e^-)$ are the mass and electronic width of the vector meson V, $x_V = 1 - m_V^2/s$, and $\mathcal{B}(V \to f)$ is the branching fraction of V into the final state f. Therefore, the measurement of the number of $J/\psi \to p\bar{p}$ decays in $e^+e^- \to p\bar{p}\gamma$ determines the product of the electronic width and the branching fraction: $\Gamma(J/\psi \to e^+e^-)\mathcal{B}(J/\psi \to p\bar{p})$. The $p\bar{p}$ mass spectra for selected events in the J/ψ and $\psi(2S)$ mass regions are shown in Fig. 21. To determine the number of resonance events, both spectra are fitted with a sum of the probability density function (PDF) for signal plus a linear background. The resonance PDF is a Breit-Wigner function convolved with a double-Gaussian function describing the detector resolution. The Breit-Wigner widths and masses for J/ψ and $\psi(2S)$ are fixed at the world-average values. The parameters of the resolution function are determined from simulation. To account for possible differences in detector response between data and simulation, the simulated resolution function is modified by adding in quadrature an additional σ_G to both σ's of the double-Gaussian function and introducing a shift of the central value of the resonance mass. The free parameters in the fit of the J/ψ mass region are the number of resonance events, the total number of nonresonant background events, the slope of background, σ_G, and the mass shift. In the $\psi(2S)$ fit the σ_G and mass shift values are fixed at those obtained for the J/ψ.

The fit results are shown as curves in Fig. 21. Numerically, we find $N_{J/\psi} = 438 \pm 22$ and $N_{\psi(2S)} = 22.2 \pm 5.7$; the number of nonresonant events is 27 ± 8 for the 3–3.2 GeV/c^2 mass interval and 7.9 ± 4.0 for the 3.6–3.8 GeV/c^2 interval. These values are used to extract the nonresonant $e^+e^- \to p\bar{p}$ cross section. Since the background subtraction procedure for nonresonant events (see Sec. IV D) uses events with $30 < \chi^2_p < 60$, the mass spectra obtained with this cut may also be fit. The numbers of J/ψ and nonresonant events are found to be 27 ± 6 and 6 ± 4. The ratio of the numbers of J/ψ events with $30 < \chi^2_p < 60$ and $\chi^2_p < 30$, 0.061 ± 0.014 is in good agreement with the value of $\beta_{p\bar{p}\gamma} = 0.048 \pm 0.003$ obtained in Sec. IV D. In the $\psi(2S)$ mass region, no events are selected with $30 < \chi^2_p < 60$. The remaining fit parameters are $\sigma_G = 4.2 \pm 1.8$ MeV/c^2 and $M_{J/\psi} - M^{\rm MC}_{J/\psi} = -(1.8 \pm 0.7)$ GeV/c^2. The fitted value of σ_G leads to a change in simulation resolution (11 MeV/c^2) of 8%.

The detection efficiency is estimated from MC simulation. The event generator uses experimental data for the angular distribution of protons in $\psi \to p\bar{p}$ decays. This distribution is described by $1 + \alpha\cos^2\vartheta$ with $\alpha = 0.660 \pm 0.045$ for J/ψ [21,22] and 0.67 ± 0.15 for $\psi(2S)$ [28]. The model error in the detection efficiency due to the uncertainty of α is negligible. The efficiencies are found to be $\varepsilon_{\rm MC} = 0.168 \pm 0.002$ for J/ψ and $\varepsilon_{\rm MC} = 0.161 \pm 0.003$ for $\psi(2S)$. The data-MC simulation differences discussed earlier are used to correct the former efficiency values by $(2.3 \pm 4.0)\%$.

The cross section for $e^+e^- \to \psi\gamma \to p\bar{p}\gamma$ for $20° < \theta^*_\gamma < 160°$ is calculated as

$$\sigma(20° < \theta^*_\gamma < 160°) = \frac{N_\psi}{\varepsilon R L},$$

yielding $(11.0 \pm 0.6 \pm 0.5)$ fb and $(0.57 \pm 0.14 \pm 0.03)$ fb for J/ψ and $\psi(2S)$, respectively. The radiative-correction factor $R = \sigma/\sigma_{\rm Born}$ is 1.007 ± 0.010 for J/ψ

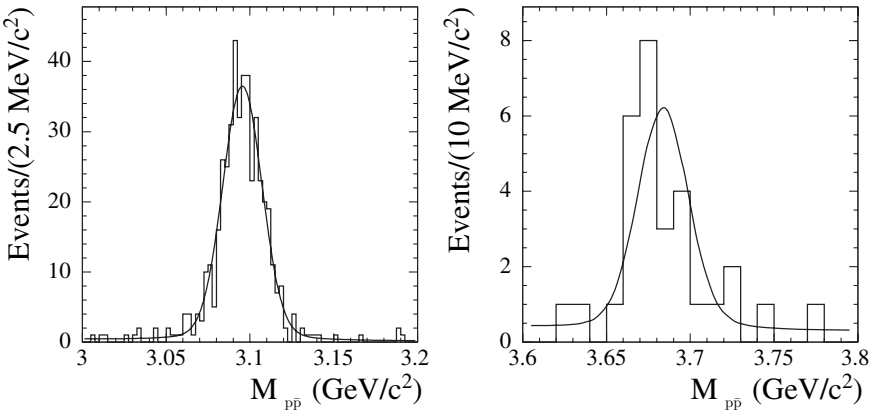

FIG. 21. The $p\bar{p}$ mass spectra in the mass regions near J/ψ (left panel) and $\psi(2S)$ (right panel). The curves are the result of the fit described in the text.

and 1.011 ± 0.010 for $\psi(2S)$, obtained from a MC simulation at the generator level.

The total integrated luminosity for the data sample is (232 ± 3) fb^{-1}. From the measured cross sections and Eq. (12), the following products are determined:

$$\Gamma(J/\psi \to e^+e^-)\mathcal{B}(J/\psi \to p\bar{p}) = (12.0 \pm 0.6 \pm 0.5) \text{ eV},$$

$$\Gamma(\psi(2S) \to e^+e^-)\mathcal{B}(\psi(2S) \to p\bar{p}) = (0.70 \pm 0.17 \pm 0.03) \text{ eV}.$$

The systematic errors include the uncertainties of the detection efficiencies, the integrated luminosity, and the radiative corrections.

Using the world-average values for the electronic widths [29], we calculate the $\psi \to p\bar{p}$ branching fractions to be

$$\mathcal{B}(J/\psi \to p\bar{p}) = (2.22 \pm 0.16) \times 10^{-3}$$

and

$$\mathcal{B}(\psi(2S) \to p\bar{p}) = (3.3 \pm 0.9) \times 10^{-4}.$$

These values are in agreement with the corresponding world-average values: $(2.17 \pm 0.08) \times 10^{-3}$ [29] and $(2.67 \pm 0.15) \times 10^{-4}$ [29–31].

IX. UPPER LIMIT ON $Y(4260) \to p\bar{p}$ DECAY

Recently, a resonantlike structure in the invariant mass spectrum of $J/\psi\pi^+\pi^-$ near 4.26 GeV/c^2 was observed by *BABAR* in the ISR process $e^+e^- \to J/\psi\pi^+\pi^-\gamma$ [13]. This structure can be characterized by a single resonance with a width of about 90 MeV and is referred to as $Y(4260)$. From the $J/\psi\pi^+\pi^-$ mass spectrum, the $e^+e^- \to Y(4260) \to J/\psi\pi^+\pi^-$ cross section at the maximum of the $Y(4260)$ resonance was found to be (51 ± 12) pb. From the fact that the $Y(4260)$ resonance is not observed in the total $e^+e^- \to$ hadrons cross section, one can conclude that $\Gamma(Y(4260) \to e^+e^-)$ is much smaller than the corresponding partial widths of all known $J^{PC} = 1^{--}$ charmonium resonances, while $\Gamma(Y(4260) \to J/\psi\pi^+\pi^-)$ is much larger [32]. The four-quark [33], hybrid [32,34], meson- or baryon-molecular [35,36] interpretations have been suggested to explain these unusual properties of the $Y(4260)$. Information about $Y(4260)$ decay modes other than $J/\psi\pi^+\pi^-$ can help clarify the nature of the $Y(4260)$ resonance. In particular, charmless decays of the $Y(4260)$ are expected in the hybrid model [32].

The $p\bar{p}$ mass spectrum is shown in Fig. 22 for $p\bar{p}\gamma$ candidates with a $p\bar{p}$ mass in the range (3.9–4.5) GeV/c^2. The mass spectrum is fit with the function

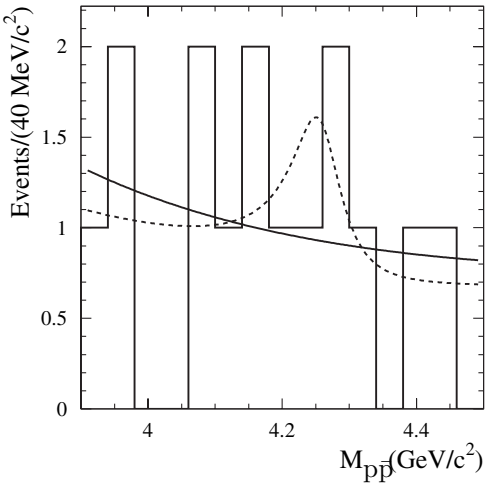

FIG. 22. The $p\bar{p}$ invariant mass spectrum for $p\bar{p}\gamma$ candidates in the (3.9–4.5) GeV/c^2 mass range. The curves are the result of the fit described in the text.

$$\frac{dN}{dm} = \frac{dL}{dm}\varepsilon R \left| \sqrt{\sigma_0(m)} + \sqrt{\sigma_Y}\frac{m_Y\Gamma_Y}{m^2 - m_Y^2 + im_Y\Gamma_Y}e^{i\phi} \right|^2 + B(m), \quad (13)$$

where $\sigma_0(m)$ is the nonresonant cross section for $e^+e^- \to p\bar{p}$, B is the contribution of background processes, σ_Y is the cross section at the maximum of the $Y(4260)$ resonance, and m_Y and Γ_Y are the resonance mass and full width, respectively. The nonresonant cross section is described by Eq. (3) with the proton effective form factor parametrized by the QCD formula $F_{p\bar{p}} = C/m^4\log^2(m^2/\Lambda^2)$ with $\Lambda = 0.3$ GeV. The total background contribution in the (3.9–4.5) GeV/c^2 mass range, mainly from $e^+e^- \to p\bar{p}\pi^0$, is estimated to be 7.5 ± 4.3 events. Because of the large uncertainty in the background, we cannot determine its slope from the fit; we assume a uniform background mass distribution. The mass and width of the $Y(4260)$ are fixed at the values obtained in Ref. [13]: $m_Y = (4259 \pm 10)$ GeV/c^2 and $\Gamma_Y = (88 \pm 24)$ GeV/c^2. The values of C, σ_Y, and the interference phase ϕ are free in the fit. The best-fit function is shown in Fig. 22 as the dashed line. The solid line represents the fit with $\sigma_Y = 0$ (null hypothesis). The optimal value of σ_Y is 2.6 pb with a significance of 0.7σ. The significance is estimated from the ratio of the values of the likelihood function for the optimal fit and the fit to the null hypothesis. Since the best-fit value of σ_Y is compatible with zero, we set an upper limit on the $e^+e^- \to Y(4260) \to p\bar{p}$ cross section.

The mass spectrum is fit with different fixed values of the interference phase ϕ and the upper limit at 90% CL is determined as a function of phase with the Neyman approach [37] using a Monte-Carlo technique. The upper limit varies from 1.0 pb to 6.4 pb. The maximum value, corresponding to $\phi = -\pi/2$, is chosen as a final result: $\sigma_Y < 6.4$ pb at 90% CL.

From the ratio of measured cross sections for $Y(4260) \to p\bar{p}$ and $Y(4260) \to J/\psi\pi^+\pi^-$, we calculate an upper limit on the ratio of branching fractions:

$$\frac{\mathcal{B}(Y(4260) \to p\bar{p})}{\mathcal{B}(Y(4260) \to J/\psi\pi^+\pi^-)} < 13\% \quad \text{at 90\% CL.} \quad (14)$$

X. SUMMARY

The process $e^+e^- \to p\bar{p}\gamma$ is studied for $p\bar{p}$ invariant masses up to 4.5 GeV/c^2. From the measured $p\bar{p}$ mass spectrum we extract the $e^+e^- \to p\bar{p}$ cross section and proton effective form factor. The form factor has a complex mass dependence. The near-threshold enhancement of the form factor observed in the PS170 experiment [10] is confirmed in this study. There are also two mass regions, near 2.25 GeV/c^2 and 3 GeV/c^2, that exhibit steep decreases in the form factor and cross section. By analyzing the proton angular distributions for $M_{p\bar{p}}$ between threshold and 3 GeV/c^2, the ratio $|G_E/G_M|$ is extracted. For masses up to 2.1 GeV/c^2, this ratio is found to be significantly greater than unity, in disagreement with the PS170 measurement [10].

From the measured numbers of $e^+e^- \to J/\psi\gamma \to p\bar{p}\gamma$ and $e^+e^- \to \psi(2S)\gamma \to p\bar{p}\gamma$ events, the products

$$\Gamma(J/\psi \to e^+e^-)\mathcal{B}(J/\psi \to p\bar{p}) = (12.0 \pm 0.6 \pm 0.5) \text{ eV},$$

$$\Gamma(\psi(2S) \to e^+e^-)\mathcal{B}(\psi(2S) \to p\bar{p}) = (0.70 \pm 0.17 \pm 0.03) \text{ eV},$$

and their corresponding branching fractions are determined:

$$\mathcal{B}(J/\psi \to p\bar{p}) = (2.22 \pm 0.16) \times 10^{-3},$$

$$\mathcal{B}(\psi(2S) \to p\bar{p}) = (3.3 \pm 0.9) \times 10^{-4}.$$

The upper limit on $Y(4260) \to p\bar{p}$ decay is obtained at 90% CL:

$$\frac{\mathcal{B}(Y \to p\bar{p})}{\mathcal{B}(Y \to J/\psi\pi^+\pi^-)} < 13\%.$$

ACKNOWLEDGMENTS

We thank V. L. Chernyak for many fruitful discussions. We are grateful for the extraordinary contributions of our PEP-II colleagues in achieving the excellent luminosity and machine conditions which made this work possible. The success of this project also relies critically upon the expertise and dedication of the computing organizations that support *BABAR*. The collaborating institutions wish to thank SLAC for its support and the kind hospitality extended to them. This work is supported by the US Department of Energy and National Science Foundation, the Natural Sciences and Engineering Research Council (Canada), the Institute of High Energy Physics (China), the Commissariat à l'Energie Atomique and Institut National de Physique Nucléaire et de Physique des Particules (France), the Bundesministerium für Bildung und Forschung and Deutsche Forschungsgemeinschaft (Germany), the Istituto Nazionale di Fisica Nucleare (Italy), the Foundation for Fundamental Research on Matter (The Netherlands), the Research Council of Norway, the Ministry of Science and Technology of the Russian Federation, and the Particle Physics and Astronomy Research Council (United Kingdom). Individuals have received support from CONACyT (Mexico), the A. P. Sloan Foundation, the Research Corporation, and the Alexander von Humboldt Foundation.

[1] G. Bonneau and F. Martin, Nucl. Phys. **B27**, 381 (1971).
[2] C. Tzara, Nucl. Phys. **B18**, 246 (1970).
[3] H. Czyz *et al.*, Eur. Phys. J. C **35**, 527 (2004).
[4] B. Delcourt *et al.* (DM1 Collaboration), Phys. Lett. B **86**, 395 (1979).
[5] D. Bisello *et al.* (DM2 Collaboration), Nucl. Phys. **B224**, 379 (1983); Z. Phys. C **48**, 23 (1990).
[6] A. Antonelli *et al.* (FENICE Collaboration), Nucl. Phys. **B517**, 3 (1998).
[7] M. Castellano *et al.*, Nuovo Cimento Soc. Ital. Fis. **14A**, 1 (1973).
[8] M. Ablikim *et al.* (BES Collaboration), Phys. Lett. B **630**, 14 (2005).
[9] T. K. Pedlar *et al.* (CLEO Collaboration), Phys. Rev. Lett. **95**, 261803 (2005).
[10] G. Bardin *et al.* (PS170 Collaboration), Nucl. Phys. **B411**, 3 (1994).
[11] T. A. Armstrong *et al.* (E760 Collaboration), Phys. Rev. Lett. **70**, 1212 (1993).
[12] M. Ambrogiani *et al.* (E835 Collaboration), Phys. Rev. D **60**, 032002 (1999); M. Andreotti *et al.*, Phys. Lett. B **559**, 20 (2003).
[13] B. Aubert *et al.* (*BABAR* Collaboration), Phys. Rev. Lett. **95**, 142001 (2005).
[14] B. Aubert *et al.* (*BABAR* Collaboration), Nucl. Instrum. Methods Phys. Res., Sect. A **479**, 1 (2002).
[15] H. Czyz and J. H. Kühn, Eur. Phys. J. C **18**, 497 (2001).
[16] M. Caffo, H. Czyz, and E. Remiddi, Nuovo Cimento Soc. Ital. Fis. **110A**, 515 (1997); Phys. Lett. B **327**, 369 (1994).
[17] E. Barberio and Z. Was, Comput. Phys. Commun. **79**, 291 (1994).
[18] T. Sjöstrand, Comput. Phys. Commun. **82**, 74 (1994).
[19] S. Agostinelli *et al.*, Nucl. Instrum. Methods Phys. Res., Sect. A **506**, 250 (2003).
[20] V. L. Chernyak (private communication).
[21] D. Pallin *et al.* (DM2 Collaboration), Nucl. Phys. **B292**, 653 (1987); R. Brandelik *et al.* (DASP Collaboration), Z. Phys. C **1**, 233 (1976); I. Peruzzi *et al.* (MARKI Collaboration), Phys. Rev. D **17**, 2901 (1978); M. W. Eaton *et al.* (MARKII Collaboration), Phys. Rev. D **29**, 804 (1984).
[22] J. Z. Bai *et al.* (BES Collaboration), Phys. Lett. B **591**, 42 (2004).
[23] G. Rodrigo *et al.*, Eur. Phys. J. C **24**, 71 (2002).
[24] M. Davier *et al.*, Eur. Phys. J. C **27**, 497 (2003).
[25] P. L. Frabetti *et al.* (E687 Collaboration), Phys. Lett. B **578**, 290 (2004).
[26] V. L. Chernyak and A. R. Zhitnitsky, JETP Lett. **25**, 510 (1977); G. Lepage and S. Brodsky, Phys. Rev. Lett. **43**, 545 (1979).
[27] M. Benayoun *et al.*, Mod. Phys. Lett. A **14**, 2605 (1999).
[28] M. Ambrogiani *et al.* (E835 Collaboration), Phys. Lett. B **610**, 177 (2005).
[29] S. Eidelman *et al.*, Review of Particle Physics, Phys. Lett. B **592**, 1 (2004).
[30] T. A. Armstrong *et al.* (E760 Collaboration), Phys. Rev. D **47**, 772 (1993).
[31] T. K. Pedlar *et al.* (CLEO Collaboration), Phys. Rev. D **72**, 051108 (2005).
[32] F. E. Close and P. R. Page, Phys. Lett. B **628**, 215 (2005).
[33] L. Maiani, V. Riquer, F. Piccinini, and A. D. Polosa, Phys. Rev. D **72**, 031502 (2005).
[34] S. L. Zhu, Phys. Lett. B **625**, 212 (2005).
[35] X. Liu, X. Q. Zeng, and X. Q. Li, Phys. Rev. D **72**, 054023 (2005).
[36] C. F. Qiao, hep-ph/0510228.
[37] J. Neyman, Phil. Trans. R. Soc. A **236**, 333 (1937).